The reuniens nucleus of the thalamus facilitates hippocampo-cortical dialogue during sleep

Diellor Basha[1,2], Amirmohammad Azarmehri[3], Eliane Proulx [1,#], Sylvain Chauvette[2], Maryam Ghorbani[3], Igor Timofeev[1,2, *]

[1]Département de psychiatrie et de neurosciences, Université Laval, Québec, QC, G1V 0A6, Canada
[2]CERVO Centre de recherche, Université Laval, Québec, QC, G1E 1T2, Canada
[3]Department of Electrical Engineering, Ferdowsi University of Mashhad, Mashhad, Iran

[#]Current address: CNS Diseases Research, Boehringer Ingelheim Pharma GmbH & Co. KG, Biberach an der Riß, Baden-Württemberg, Germany

*Lead contact and correspondence: igor.timofeev@fmed.ulaval.ca

Summary

Memory consolidation during sleep depends on the interregional coupling of slow waves, spindles, and sharp wave-ripples (SWRs), across the cortex, thalamus, and hippocampus. The reuniens nucleus of the thalamus, linking the medial prefrontal cortex (mPFC) and the hippocampus, may facilitate interregional coupling during sleep. To test this, electrophysiological recordings were obtained in vivo from the cat reuniens nucleus, prefrontal cortex and hippocampus. Interregional synchrony was measured using phase-amplitude coupling and interregional time delays between SWRs, spindles and slow waves together with reuniens spiking and local field potential (LFP) activity. Electrical stimulation of the reuniens evoked intracellular mPFC responses, consistent with bidirectional functional connectivity between mPFC-reuniens and hippocampus. Cortical slow waves preceded reuniens slow waves and hippocampal SWRs. Hippocampal SWRs and REM sleep theta modulated reuniens activities

and reuniens spindles preceded cortical spindles. The neural mass model of this network demonstrates that the strength of bidirectional hippocampo-thalamic connections determines the coupling of oscillations, suggesting a mechanistic link between synaptic weights and the propensity for interregional synchrony.

Impact Statement

The nucleus reuniens of the thalamus play a central role in synchronizing the mPFC-hippocampal network during sleep and integrates converging activity from hippocampal and mPFC oscillations.

Keywords

Nucleus reuniens, hippocampus, medial prefrontal cortex (mPFC), slow waves, sleep, spindles, sharp wave-ripples (SWRs), interregional synchrony, neural mass model, phase amplitude coupling

Introduction

Interactions between the hippocampus and the medial prefrontal cortex (mPFC) are essential for cognition. During sleep, hippocampal and cortical activity is continually synchronized by cardinal sleep oscillations such as slow waves (SWs, 0.1-4 Hz), thalamocortical spindles (10-15

46 Hz), and hippocampal sharp-wave ripples (SWRs, 100-300 Hz) [1,2]. These rhythms have well-
47 known roles in neuronal plasticity [3,4] and in the consolidation of hippocampus-dependent
48 memories [5]. In particular, the hierarchical coupling of slow waves, spindles and SWRs is thought
49 to promote the stabilization of short-term memory [4]. Consistent with this hypothesis, the
50 temporal coupling of hippocampal and mPFC sleep oscillations results in a selective increase in
51 the recall of hippocampus-dependent memory[5,6].

52 At present, the pathways that coordinate the long-range coupling of slow waves, spindles and
53 SWRs across the prefronto-hippocampal network are not well characterized. Although the
54 hippocampus extends projections to several prefrontal areas[7-11], few regions of the prefrontal
55 cortex reciprocate[12]. With respect to medial regions of the prefrontal cortex, no direct
56 projections to the hippocampus have been identified[11,13-16].

57 The nucleus reuniens of the thalamus (reuniens) is bidirectionally connected to the
58 hippocampus and the mPFC[17,18], making it an ideal hub for coupling hippocampo-cortical
59 interactions during sleep. Reuniens is part of the ventral group of midline thalamic nuclei with
60 widespread connections to cortical, thalamic, hypothalamic and brainstem structures [18-22].
61 Consistent with its anatomical connections to the hippocampus and the mPFC, reuniens is
62 required for memory function[23,24] and a growing body of evidence points its critical role in
63 processing hippocampus-dependent memory [23,25]. Although evidence for the functional
64 significance of reuniens in cognitive operations is strong, little is known about the nature of
65 reuniens-prefrontal interactions and their interplay with hippocampal events during sleep [26].

66 Considering the well-established link between sleep and memory consolidation [4,27,28], we
67 investigated the role of the reuniens in coupling hippocampo-cortical oscillations during non-
68 rapid eye movement (NREM) and REM sleep. Using in vivo intracellular recordings,
69 computational modelling, and spike/local field potential (LFP) recordings, we demonstrate that
70 reuniens is driven by hippocampal oscillations during sleep and that it elicits fast, consistent
71 synaptic responses in mPFC. Hippocampal and reuniens activity precedes the onset of mPFC
72 spindles, suggesting a hippocampo-thalamic trigger for spindle initiation. In turn, the phase of
73 mPFC slow waves determined the amplitude of reuniens spindles and of SWR timing, forming a
74 functional feedback loop through the reuniens.

75 Results

76 Reuniens elicits fast, consistent synaptic responses in the mPFC

77 We obtained intracellular recordings of mPFC neurons in vivo (n=49 neurons) during targeted,
78 electrical stimulation of the ventral hippocampus and reuniens in anesthetized cats (Figure 1A-
79 D). Stimulation of the hippocampus and reuniens elicited synaptic responses in 55% and 51% of
80 recorded mPFC neurons, respectively. Hippocampal stimulation generated variable responses in
81 the same neurons, consisting of complex sequences of either two excitatory postsynaptic
82 potentials (EPSPs) followed by long-lasting hyperpolarization (Figure 1E, top, left), a
83 depolarization-hyperpolarization sequence (Figure 1E, middle, left), or no response (Figure 1E,
84 bottom, left). The polarity of early depolarizing responses elicited by hippocampal stimulation
85 was dependent on membrane potential, reversing with progressive depolarization of the

86 membrane at around -70 mV (Figure 1E, right), suggesting that the initial depolarization was an
87 inhibitory postsynaptic potential (IPSP).

88 Reuniens stimulation elicited consistent EPSPs followed by long-lasting hyperpolarization
89 (Figure 1C, bottom) at earlier latencies than hippocampal stimulation (Figure 1G). EPSPs elicited
90 by reuniens stimulation had faster rising slopes compared to hippocampal stimulation (mean ±
91 SD) but were of lower amplitude. We observed no significant difference in the duration of the
92 late, hyperpolarizing component in response to reuniens and hippocampal stimulations.

93 Reuniens stimulation elicited action potentials that were either orthodromic (85%), antidromic
94 (10%) or both (5%), evidenced by jitter in the latency of orthodromic action potentials and
95 consistent latency of antidromic action potentials (Figure 1F). Antidromic responses to reuniens
96 stimulation, confirmed by collision tests, were recorded in cells located 6050-6600 μm ventral
97 to the dorsal aspect of the cortical surface. The mean latency of antidromic spikes was 2.9±0.25
98 ms (mean ± SD).

99 To characterize the prefrontal topography of reuniens and hippocampal receptive fields, we
100 descended a 4-shank microelectrode array into the mPFC in 1 mm steps and recorded evoked
101 field potentials in response to reuniens and hippocampal stimulation (Figure 1H). Reuniens
102 stimulation evoked field postsynaptic potential in a wider prefrontal territory compared to
103 hippocampal stimulation which was restricted to the ventromedial wall of the mPFC. In some
104 locations of mPFC, early responses to reuniens stimulation (Figure 1 H, I) corresponded to
105 criteria of field potential antidromic responses[29]. Areas in the prefrontal cortex that responded
106 to hippocampal stimulation overlapped with areas exhibiting antidromic responses to reuniens

107 stimulation (Figure 1 I, shadowed area). In the following experiments, we targeted this region
108 of the mPFC.

109 Reuniens and hippocampal activity precede the onset of mPFC spindles

110 Sleep enhances communication in the hippocampo-cortical pathway by promoting interregional
111 synchrony through highly rhythmic events such as slow waves and spindles. To investigate the
112 role of the reuniens in mediating synchrony in the mPFC-hippocampal network, we performed
113 LFP recordings of the mPFC and hippocampus, as well as targeted spike/LFP recordings of the
114 reuniens during natural sleep (Figure 2A, Figure 2 – figure supplement 1). Recordings were
115 segmented into wake, NREM and REM epochs, based on mPFC delta power, mPFC signal
116 amplitude, and nuchal muscle activity (Figure 2 B-D). During NREM sleep, LFP recordings and
117 corresponding wavelet transforms of the signal suggested correlated activity among mPFC slow
118 waves, spindles, hippocampal SWRs, and reuniens multi-unit activity (Figure 2E). We observed
119 co-occurring reuniens and mPFC spindles (Figure 2F), characterized by significantly earlier onset
120 of reuniens spindles relative to the onset of mPFC spindles (Figure 2G).

121 Analysis of reuniens single-unit activity relative to the phase of mPFC and reuniens spindle
122 cycles revealed significant phase-locking of reuniens single-units to mPFC spindle cycles and
123 reuniens spindle cycles (Figure 2H, 2I). The mean phase preference of reuniens single-units was
124 advanced for reuniens spindle cycles relative to mPFC spindle cycles. For pairs of co-occurring
125 reuniens and mPFC spindles, spindle amplitudes were significantly correlated (Figure 2J, 2K).

126 Lastly, we investigated the change in hippocampal and reuniens signal power during mPFC
127 spindles relative to baseline, which demonstrated increased hippocampal ripple power and

128 increased reuniens spindle power preceding the onset of spindles in the mPFC (Figure 2L, top).
129 The histogram of SWR incidence in the same time window, referenced to the onset of mPFC
130 spindles, indicated increased SWR incidence prior to the onset of mPFC spindles (Figure 2L,
131 middle). Reuniens multi-unit activity increased prior to the onset of mPFC spindles (Figure 2L,
132 bottom).

133

134 mPFC slow waves determine spindle amplitude in the reuniens-mPFC 135 network

136 To examine the modulation of reuniens and hippocampal activity by mPFC slow waves, we
137 analyzed the relationship between the phase of mPFC slow waves with respect to spindles and
138 SWRs. Figure 3A shows a representative example of a coupled slow wave-spindle event from
139 simultaneous recordings of the mPFC and reuniens. We analyzed the average time-frequency
140 representation of mPFC amplitudes locked to the peak of the mPFC slow wave (Figure 3B), as
141 well as the average time-frequency representations of reuniens amplitudes, locked to the peak
142 of the same mPFC slow waves (Figure 3C), which showed significant modulation of spindle
143 amplitudes by the phase of the mPFC slow wave.

144 The strength of slow wave-spindle coupling, estimated by the absolute value of the
145 synchronization index was higher for mPFC slow wave-reuniens spindle coupling compared to
146 mPFC slow wave-mPFC spindle coupling (Figure 3 D). A comparison of slow wave-spindle
147 coupling strength between mPFC-mPFC pairs and mPFC-reuniens pairs is shown in Figure 3E.
148 The amplitude of reuniens spindles increased at earlier phases of the mPFC slow wave

149 compared to the amplitude of mPFC spindles, which increased at later phases of the mPFC slow
150 wave (Figure 3B,C,F).

151 Next, we examined the relative delays in the timing of mPFC and reuniens slow waves. Figure
152 3G shows a representative example of an overlapping mPFC and reuniens slow wave, with
153 circles indicating slow wave peaks. Single session data in Figure 3H demonstrates the delay
154 between reuniens and mPFC slow waves, showing significant lag in the time of reuniens slow
155 waves relative to mPFC slow waves. The distribution of median delay times for all recording
156 sessions between each reuniens-mPFC slow wave pair are shown in Figure 3I.

157 Lastly, we analyzed the phase-locking of hippocampal SWRs to mPFC slow waves. Figure 3J
158 shows a representative example of a coupled slow wave-SWR event. The distribution of slow
159 wave phases at the time of SWRs was non-uniform, indicating significant phase-locking of SWRs
160 to mPFC slow waves at a mean phase of 162.7° (Figure 3K). We found no significant phase-
161 locking of SWRs to spindle cycles in the majority of recording sessions (n=3/51 with significant
162 phase for mPFC spindle-SWR and n=10/51 sessions with significant phase for reuniens spindle-
163 SWR coupling, Figure 3 – figure supplement 1 and Table 1).

164 Hippocampal oscillations modulate reuniens activity

165 Considering the comodulation of reuniens and hippocampal activity prior to mPFC spindles, we
166 asked whether hippocampal oscillations directly influence firing activity in the reuniens. A
167 representative example of LFP recordings of the hippocampus, mPFC, and reuniens during REM
168 sleep is shown in Figure 4A. The wavelet spectrogram of the hippocampal trace demonstrates
169 prominent theta-band activity during REM with periodic locking of reuniens multi-unit activity

170 to hippocampal theta cycles (Figure 4B). Analysis of reuniens firing around the peak of
171 hippocampal theta cycles, shows significant phase-locking of reuniens single-unit activity to the
172 theta rhythm during REM (Figure 4C-F).

173 Power spectra of mPFC, reuniens, and hippocampal signals during REM are characterized by
174 prominent peaks in the theta range, with coherence between mPFC-hippocampus, reuniens-
175 hippocampus, and mPFC-reuniens recording pairs in the theta range during REM (Figure 4 G, H).
176 mPFC-reuniens recordings were further comodulated by a slow, irregular potential observed in
177 Figure 4A and in the broad low frequency peak (Figure 4H, bottom). Cross-correlations and
178 relative time lags of reuniens-hippocampus and mPFC-hippocampus recording pairs during REM
179 are illustrated in Figure 4I. mPFC signals lagged hippocampal signals by a longer delay than
180 reuniens signals lagged hippocampus (Figure 4J, top) and peak cross-correlation coefficients
181 were significantly higher for reuniens-hippocampus recording pairs than for reuniens-mPFC
182 (Figure 4J, bottom).

183 Next, we analyzed reuniens firing activity during SWRs in NREM. Figure 4K shows representative
184 LFP recordings of the hippocampus and reuniens multiunit activity during SWR events in NREM
185 sleep. In 20.4 % of reuniens single-units (10/49), firing rate increased significantly following the
186 onset of SWRs in the hippocampus, compared to shuffled events in the same period (Figure 4L,
187 150 ms post-SWR onset). Firing rates decreased significantly in 32.6% (16/49) of single-units
188 following SWR onset The average thalamic LFP around the onset of the SWR was characterized
189 by a negative, 250 μV deflection coincident with increased reuniens firing.

Hippocampal-thalamocortical model

To explore the parameters that control interregional synchrony during NREM sleep, we constructed a neural mass firing rate model consisting of two cortical networks (N 1 & 2), representing mPFC layers 5 and 6, respectively, and two hippocampal (CA1-CA3) and three thalamic networks (TRN, MD, and Reu, Figure 5A). Slow waves and sharp waves are spontaneously generated in the isolated CA3 and cortical networks respectively as a result of adaptation and excitatory-to-excitatory recurrent connections. SWRs are reproduced in the CA1 network during the active phase of the sharp wave due to recurrent connections between the CA1 excitatory and inhibitory neurons with the firing rates sharply dependent on the membrane potential in this firing rate model [30]. The oscillations in the range of spindle frequency are spontaneously generated in the bursting, recurrently connected MD-TRN network. The beginning and end of the spindles are controlled by cortical inputs in the thalamocortical model with long-range bidirectional projections between cortical and thalamic networks. In the full hippocampo-cortico-thalamic model, the CA1 is directly connected to the cortical network while reuniens, which is bidirectionally connected to both CA1 and cortical networks, mediates the cortical to CA1 influence. With large enough strength of multi-regional projections, the model can spontaneously reproduce the experimentally observed coupling between the slow waves, spindles, and SWRs (Figure 5B). We found that reuniens slow waves occur significantly later than cortical slow waves (Figure 5C). In contrast, thalamic spindles occur significantly earlier than cortical spindles (Figure 5D).

Figure 5E shows the average of cortical slow wave trough-locked time-frequency representations of the membrane potential of mPFC excitatory neurons and reuniens neurons. The slow wave-spindle coupling angles are nonuniformly distributed for both cortical and reuniens spindles indicating strong coupling with slow waves. In quantitative match to the experimental data, reuniens spindles occur mainly around the slow wave peak (active phase) while cortical spindles mainly occur around the slow wave trough. The slow wave-spindle coupling strength is also higher for reuniens than cortical spindles (Figure 5F). Slow waves in the thalamocortical network are also accompanied by large negative deflections and a subsequent peak in CA1 network (Figure 5G). Phase locking analysis revealed that, consistent with the experimental data, SWRs are phase-locked to slow waves, occurring mainly before slow wave peaks (active phase, Figure 5H). The bidirectional projections between reuniens and CA1 coordinate the communication between these two networks so that the membrane potential of the reuniens neurons increases after SWRs (Figure 5I). Reuniens spindles were also preceded by an increase in the SWR rate (Figure 5J, the peak SWR rate occurs 0.32 s before the spindle onset).

Bidirectional projections between the reuniens and CA1 control multiregional interactions

To investigate how bidirectional projections between the reuniens and CA1 control multiregional interactions in the model, we explored hippocampal-thalamocortical coupling during sleep rhythms as a function of the strength of bidirectional projections between reuniens and CA1. The correlation between reuniens and CA1 membrane potentials during

231 SWRs increased by increasing the strength of CA1 to REU projections (Figure 6A). In addition,
232 the SWR activity before spindle onset is an increasing function of bidirectional projections
233 between CA1 and reuniens (Figure 6B). Next, we studied the effect of the strength of reuniens-
234 CA1 bidirectional projections on CA1 activity during cortical slow waves. The peak-to-trough
235 magnitude of CA1 deflections around the cortical slow wave also increases by increasing the
236 reuniens-CA1 bidirectional projections (Figure 6C). The slow wave mean phase at the time of
237 SWR occurrence decreased by increasing the strength of the bidirectional projections between
238 reuniens and CA1 so that SWRs mostly occur before and after slow wave peak for strong and
239 weak projections, respectively (Figure 6D). These results suggest that for strong reuniens-CA1
240 projection, the depolarizing input from reuniens during down-to-up transition is large enough
241 to induce the SWRs in CA1 before the slow wave peak. Further, slow wave phases at the time of
242 SWR occurrence are more nonuniformly distributed for stronger CA1-reuniens projection,
243 indicating stronger phase locking of SWRs to slow waves.

244 Discussion

245 This study examined the functional relationship between mPFC, reuniens, and hippocampal
246 activity in cats using electrophysiological and computational approaches. We found that
247 reuniens activity during natural sleep was strongly modulated by hippocampal oscillations, and
248 that reuniens-mPFC spindles were preceded by increased probability of hippocampal SWRs and
249 ripple power. Electrical stimulation of reuniens generated orthodromic and antidromic spiking
250 in mPFC neurons, indicating bidirectional thalamocortical circuitry between the mPFC and
251 reuniens. Slow waves in reuniens lagged prefrontal slow waves but spindles in reuniens led

252 prefrontal spindles, suggesting a bidirectional, oscillation-dependent dialogue between
253 reuniens and the mPFC. Spindle amplitude and SWR occurrence was modulated by the phase of
254 the prefrontal slow oscillation, consistent with the idea that prefrontal slow waves control the
255 timing of thalamic and hippocampal events. Overall, the study provides physiological
256 confirmation to the hypothesis that reuniens is a core mediator in hippocampo-cortical
257 dialogue.

258 Hippocampal influence on the activity of prefrontal neurons is a central mechanism in sleep-
259 dependent memory consolidation [31-33]. Previous research has shown that response latency in
260 the hippocampo-prefrontal pathway exhibits substantial variability [34], indicating the
261 involvement of both monosynaptic and polysynaptic mechanisms in prefrontal response to
262 hippocampal input. Our findings support this notion, as we observed inconsistent mPFC
263 responses to hippocampal stimulation, occurring later than those elicited by reuniens
264 stimulation. Notably, the same cell in mPFC could respond or not respond to hippocampal
265 stimuli (Figure 1 C, E) while LFP responses were less variable. This was possibly due to
266 inhibitory mechanisms such as shunting/feedforward inhibition or cholinergic, monoaminergic,
267 or thalamic gating mechanisms [35-40].

268 While the functional impact of the hippocampo-prefrontal pathway has been extensively
269 studied, there are fewer studies on the effects of reuniens on the prefrontal cortex [26]. In our
270 study, half of recorded prefrontal cells responded to reuniens stimulation, with a mean
271 response latency of 6 ms and with antidromic spikes with a latency of approximately 3 ms,
272 pointing to bidirectional functional connectivity between the two structures. Similarly, electrical

273 stimulation of the reuniens/rhomboid nucleus in rats [26] elicits prominent evoked potentials in
274 prefrontal cortices that have putatively monosynaptic latencies of 4.5 ms. We found that mPFC
275 responses to reuniens stimulation were qualitatively different from responses elicited by
276 hippocampal stimulation, with significant differences in latency, amplitude, slope of EPSPs, and
277 duration of hyperpolarization. Reuniens-evoked responses occurred earlier and were more
278 consistent than hippocampal-evoked responses, suggesting higher response fidelity in the
279 reuniens-prefrontal pathway than in the hippocampo-cortical pathway. Both pyramidal cells
280 and inhibitory neurons mediate the hippocampo-prefrontal response, with the early
281 component thought to be primarily mediated by AMPA receptors [34,41] and the early
282 hyperpolarization was likely mediated by $GABA_A$ and the late component by either $GABA_B$
283 conductances [34] or it was mediated by disfacilitation[42,43]. Interneurons also respond to
284 hippocampal stimulation, with a shorter response latency than pyramidal cells, suggesting that
285 the hippocampus can exert feedforward inhibition in the medial prefrontal cortex [44]. AMPA
286 receptors and GABA inhibition may also mediate the primary and hyperpolarizing responses to
287 reuniens stimulation in medial prefrontal cells as in the mediodorsal-prefrontal pathway [45].
288 Similar to hippocampal afferents to the mPFC, the reuniens nucleus extends glutamatergic
289 afferents to the prefrontal cortex [46,47] and exerts a strong influence on the prefrontal activity.

290 Reuniens is believed to play a critical role in connecting the prefrontal cortex and hippocampus
291 due to its bidirectional connections with both structures [26]. The prefrontal cortex and
292 hippocampus are both essential for memory processing [31], and previous research indicates the
293 reuniens may synchronize the activity of these two structures [48]. Demonstrations that the
294 nucleus reuniens exerts excitatory actions at the CA1 [49,50] and also at the prefrontal cortex [26]

295 (intracellularly confirmed and described in our study) provides supporting evidence for this
296 claim. We also found that hippocampal stimulation evoked strong responses in cortical areas
297 coincident with the recording site of antidromic responses to reuniens stimulation (Figure 1).
298 These results support the idea that the reuniens nucleus, hippocampus, and prefrontal cortex
299 form a functional loop, with the prefrontal cortex acting as a mediator of the hippocampo-
300 prefronto-thalamic relay.

301 In NREM sleep, the coupling of hippocampal SWRs to cortical slow waves and thalamocortical
302 spindles is thought to be the main network mechanisms by which the brain promotes the
303 consolidation of short-term memory into long-term storage [5,27]. However, the mechanism that
304 govern the emergence of this interregional synchrony remain unclear. We found that reuniens
305 single-unit activity exhibited sporadic locking to hippocampal theta cycles and was strongly
306 modulated by hippocampal SWRs. Considering the strong influence of reuniens on prefrontal
307 targets, the hippocampal modulation of reuniens activity points to a thalamic pathway for the
308 coupling of sleep rhythms. Although the minimal requirement to generate spindles is the
309 reticular thalamic nucleus (TRN) [51,52] , our finding of increased SWR probability and ripple
310 power prior to the onset of thalamocortical spindles suggest that hippocampal drive through
311 reuniens may initiate the thalamocortical cascade of events that leads to spindles.

312 In first-order nuclei of the thalamus, cortical firing can trigger spindles by exciting
313 hyperpolarized neurons of the TRN, eliciting high-frequency spike bursts[53]. In turn, TRN bursts
314 can drive IPSPs in thalamocortical neurons, eliciting low-threshold calcium spikes [51] and
315 developing the spindle primarily through recurrent inhibitory-excitatory interactions between

316 the TRN and thalamocortical neurons[53]. Cortical firing also contributes to spindle
317 synchronization and the maintenance of the spindle through its influence on the TRN [54]. Thus,
318 cortical activation after the down state can initiate thalamocortical spindling and lock the
319 timing of spindles to the phase of the slow oscillation. However, less is known about spindle
320 generation in higher-order thalamic nuclei, especially in thalamic nuclei with limbic circuitry
321 such as reuniens. In general, although first order thalamocortical cells display inhibitory,
322 spindle-like activities during cortical active state, higher order thalamocortical cells show
323 persistent depolarizing states, excluding their possibility to generate spindle-related rebound
324 spike bursts[55,56]. The bidirectional connections of the reuniens to neocortical and archicortical
325 structures make it difficult to discern the possible triggering event that initiates the spindle in
326 this nucleus. We found that hippocampal SWRs trigger thalamic firing and precede the onset of
327 reuniens and mPFC spindles, which points to SWRs as possible candidate events for spindle
328 initiation. In this regard, the strong excitatory drive emerging form the hippocampus during
329 SWRs may represent an ontogenetically different mechanism for the initiation of spindles in the
330 limbic circuitry. However, the generation and maintenance of spindle cycles depend on burst
331 firing from inhibitory structures such as the TRN. To date, it is not yet clear whether the
332 hippocampus influences inhibitory thalamic structures such as the TRN or the zona incerta,
333 although projections from subiculum to the rostral TRN were previously described[57]. We
334 propose that hippocampal SWRs can initiate a cascade of thalamocortical events, beginning
335 with the excitation of reuniens, which in turn excites the mPFC. This mPFC excitation leads to
336 spindle activity generated through cortico-thalamic feedback from the mPFC to other thalamic
337 nuclei, such as the MD nucleus.

338 Our computational model demonstrates the presence of cross-regional interactions
339 between the prefrontal cortex and its thalamic partners. The model confirmed that thalamic
340 slow waves occur significantly later than cortical slow waves, whereas thalamic spindles occur
341 significantly earlier than cortical spindles, recapturing our experimental findings and pointing to
342 the cortical origin of slow-wave activity and thalamic origin of spindles. The model predicts that,
343 while CA1 to reuniens connection strength plays a critical role in the modulation of reuniens
344 activity by SWRs, bidirectional connections between reuniens and CA1 are critical for SWR-
345 dependent triggering of spindles. Similarly, bidirectional reuniens and CA1 connections are
346 important for transmitting cortical slow wave activity to the CA1 region. With strong
347 bidirectional connections, the SWR occurred primarily before the slow wave active phase peak
348 and with weak connections, the SWR tended to occur after this peak. Given our experimental
349 findings (Figure 3, J-K) the model suggests that the effectiveness of bidirectional connections
350 between reuniens and CA1 is particularly strong during NREM in cat.

351 Materials and Methods

352 Experimental model and subject details

353 Experiments were carried out in accordance with the guidelines of the Canadian Council on
354 Animal Care and were approved by the Committee for Animal Care of Université Laval and are
355 consistent with ARRIVE guidelines. In 20 adult cats (16 anesthetized during recording sessions
356 and 4 chronically implanted, not anesthetized during recording sessions), aged 1-1.5 years,
357 electrophysiological recordings were obtained from the mPFC, midline thalamus, hippocampus

and/or various cortical areas including somatosensory, motor, auditory, associative, and visual cortex. Prefrontal intracellular recordings (n=20) and LFP-array recordings (n=9) were obtained from anesthetized animals and spike/local field potential (n=4) recordings were obtained from non-anesthetized animals during sleep and wake cycles.

Surgeries

Anesthetized Animals

For acute intracellular recordings, cats were anesthetized with a mixture of ketamine and xylazine (10-15 and 2-3 mg/kg i.m., respectively) and maintained in anesthetic state during the experiment by supplemental doses of ketamine (5 mg/kg). Body temperature was maintained at 37°C via a feedback-controlled heating pad and the heart rate was continuously monitored (90-110 bpm). All pressure points and incision sites were infiltrated with lidocaine (0.5%). Animals were paralyzed with gallamine triethiodide and artificially ventilated to an end-tidal CO_2 concentration of 3.5-3.8%. Recording stability was maintained by cannulation of the cisterna magna, bilateral pneumothorax, hip suspension, and by sealing craniotomies with agar solution (4% in 0.9% saline).

Non-anesthetized animals

For chronic spike/LFP recordings, cats were implanted with indwelling electrodes and a head-restraint system according to surgical procedures described previously in Timofeev et al. [59] and Chauvette et al. [60]. Briefly, cats were pre-anesthetized with an intramuscular injection of ketamine (3 mg/kg), buprenorphine (0.02 mg/kg), and dexmedetomidine (5 µg/kg). The incision site was shaved, and the cats were intubated for gaseous anesthesia. Lidocaine (0.5%) and

379 bupivacaine (0.25%) was injected at the site of the incision and in all pressure points where the
380 head contacted the stereotaxic frame. Four stainless-steel electrodes were implanted under
381 stereotaxic guidance in the mPFC (*from the interaural line: AP 23 to 24 mm, ML 1 mm, DV 5*
382 *mm, ϑ=10°*) according to the Reinoso-Suarez stereotaxic atlas of the cat brain [61]. Additionally,
383 single stainless-steel electrodes were implanted in deep cortical layers (1.2 mm from cortical
384 surface) in the ipsi- or contralateral hemisphere in the marginal gyrus [visual cortex (areas 17
385 and 18)], suprasylvian gyrus [associative cortex (areas 5, 7, and 21)], ectosylvian gyrus [auditory
386 cortex (areas 22 and 50)], postcruciate gyrus [somatosensory cortex (area 3)], precruciate gyrus
387 [motor cortex (areas 4 and 6)]. Tetrodes, constructed out of four twisted microwires (platinum-
388 iridium, 12.5 µm, gold-plated to ~200 kΩ), were implanted into the midline thalamus (*from the*
389 *interaural line: AP 11.5, ML 0.5, DV 1.5, ϑ=10°*) and into the CA1 region of the hippocampus
390 (*from the interaural line: AP 7, ML 10.5, DV -3.5, ϑ=10°*).

391 For electro-oculography (EOG), a silver electrode was implanted through the orbital bone and
392 for electromyography (EMG), two teflon-insulated stainless-steel electrodes were implanted
393 into the neck muscle. All recordings were referenced to a silver electrode fixed to the skull
394 above the cerebellum. To allow for subsequent head-restrained recordings, head-fixation
395 holders were also attached and encased into the dental cement. Throughout the surgery, the
396 body temperature was maintained at 37°C using a water-circulating thermo-regulated blanket.
397 Heartbeat, oxygen saturation and blood pressure were continuously monitored using a pulse
398 oximeter (Rad-8; MatVet), and the level of anesthesia was adjusted to maintain a heartbeat at
399 130-150 per minute. Lactate Ringer's solution was given intravenously (5 ml/ kg/h, i.v.) during
400 the surgery. After the surgery, cats received meloxicam (0.05 mg/kg) once a day for 3 days.

Electrophysiological recordings

Acute recordings in anesthetized animals

Intracellular recordings of the mPFC were obtained in vivo using glass micropipettes pulled on a vertical puller (Narishige PP-830, Tokyo, Japan) from borosilicate capillary tubes (WPI; P-97, Sutter Instrument) and filled with 3 M potassium acetate (DC resistances of 30- 60 MΩ). The prefrontal region around the cruciate gyrus was targeted according to the stereotaxic cat atlas of Reinoso-Suárez [61] (*from the interaural line: AP 23 to 24 mm, ML 1 mm, DV 5-14.5 mm)*. The micropipette was advanced dorsoventrally until a cell was penetrated, confirmed *in situ* by electrophysiological observations and classification. A high-impedance amplifier (Neurodata IR-283 amplifiers; Cygnus Technology) with active bridge circuitry was used to record the membrane potential (sampled at 20 kHz) and to inject current into neurons.

Stimuli (0.2 ms, 0.3-1.5 mA) were delivered in single pulses at 1 Hz through bipolar (coaxial) electrodes implanted in the ventral midline thalamus (*from the interaural line: AP 12, ML 0.0, DV 1.0*) and hippocampus (*from the interaural line: AP 7.2, ML 10.5, DV -4.5)*. Bandpassed (0.1 Hz-10 kHz) field potentials were recorded through the same bipolar electrodes at 20 kHz sampling.

To study the topography of prefrontal responses to thalamic and/or hippocampal stimulation, an array of 4 tungsten microelectrodes (9-12 MΩ) was positioned in the mPFC in 9 animals. The array was positioned close to the midline in the pericruciate gyrus sigmoidus and advanced ventrally in 1 mm steps. At each step, thalamic or hippocampal stimuli (0.2 ms, 0.3-1.5 mA) were delivered at 1 Hz or in 5-pulse trains every 2 seconds at 5Hz, 10Hz, 20 Hz and 100 Hz

through bipolar (coaxial) electrodes implanted in the ventral midline thalamus (*from the interaural line: AP 12, ML 0.0, DV 1.0*) and hippocampal formation (*from the interaural line: AP 7.2, ML 10.5, DV -4.5)*. Antidromic events were detected according to methods described previously in Lipski [62].

To label stimulation sites, electrolytic lesions were made through thalamic and hippocampal electrodes via 0.75 mA, 1 s current pulses, delivered every 3 s for 5 minutes.

Chronic recordings in non-anesthetized animals

For non-anesthetized cats, a post-operative recovery time of 1 week was maintained prior to the first recording session. Cats were trained over 2-3 days to remain in head-restrained position for 2– 4 h and cycle through periods of quiet wakefulness, NREM, and REM sleep. Recordings were obtained over two weeks following the post-operative recovery period. All recordings were conducted within a Faraday chamber using AM 3000 amplifiers (A-M Systems), bandpassed 0.1 Hz to 10 kHz with a 1k gain. All signals were sampled at 20 kHz and digitized with PowerLab (ADInstruments - Data Acquisition Systems for Life Science, RRID:SCR_001620).

Histology

At the conclusion of experiments, animals were deeply anesthetized and perfused intracardially with 4°C saline (0.9%) followed by 4% paraformaldehyde (PFA) in 0.1 M phosphate buffer in saline (PBS). Brains were extracted and cryoprotected by immersion in several sucrose-PFA solutions of increasing sucrose concentration (10, 20 and 30% sucrose in PFA over 1 week). Brains were then sectioned in a freezing microtome (80 or 100 µm thickness), mounted on gelatinized glass slides, dried, and subsequently labelled with DAPI (300 nM, Invitrogen D3571)

or stained with cresyl violet by standard Nissl-staining procedures. The coverslipped sections were visualized in brightfield (Nissl) or fluorescence (DAPI) microscopy and sections with electrode tracks were photographed in 10 and 20 x magnification.

Analysis

Signals were analyzed using Igor Pro 4.0 (Wavemetrics, Inc.), built-in and custom routines in Spike2 (Cambridge Electronic Design, Ltd.) and custom-written and open-source code in MATLAB (Mathworks Inc.)

Intracellular data analysis

Stimuli were detected manually, and minimal binomial smoothing was performed to diminish noise on occasion. The latency of orthodromic responses was calculated as the time when the response reached 10% of the maximal amplitude of the sigmoidal fit of the rise of the EPSP. The amplitude of the EPSP was calculated as the maximum of this sigmoidal fit, and the slope of the EPSP calculated as the maximum of the differentiation of this fit. A horizontal line was drawn across the response from the base of the early EPSP and the interception of this line by the hyperpolarizing potential was used to calculate the duration of this latter component. Responses to sweeps of five pulse stimulation trains were averaged with an IgorPro algorithm (n=30 per stimulation protocol). The EPSP response magnitude elicited by the stimulation of the reuniens nucleus was computed by computing the area below the curve. Average response areas evoked by pulses 2 through 5 of the train were subsequently normalized by dividing by the response evoked by the first pulse.

Wake, NREM and REM detection

Detection of wake, NREM and REM sleep was based on automated analysis of the mPFC and EMG signals, followed by manual REM scoring using mPFC, EMG and EOG data. For automated detection, the Spike2 script RatSleepAuto, based on rodent recordings [63], was adapted to cat mPFC recordings. Briefly, the mPFC signal was downsampled to 100 Hz and bandpassed in the delta range (1-4 Hz). The mPFC, EMG and the delta-filtered mPFC signals were then squared and the mean of each signal was calculated in 5 second bins. Each 5-second bin was classified as NREM if the mPFC and delta signals exceed the mean + 1 standard deviation (SD) of the signal and if the EMG fell below mean - 1 s.d. All bins other than NREM were initially classified as wake. In the subsequent manual correction, “wake” bins with EMG below mean – 1 s.d. and EOG above mean + 1 s.d. were classified as REM. In the final stage, the 5-second bins were combined into groups of 4 to create 20 second epochs of wake, REM or NREM according to the majority of 5-second bins that comprised the 20 second epoch. Epochs without a majority of either NREM, REM or wake were labelled as “Transition”.

Slow wave, spindle and SWR detection

Slow wave, spindle and SWR detection was based on methodology described previously in Alizadeh et al. [64] and respectively in Zugaro et al. [65], Klinzing et al. [66] and Levenstein et al. [67]. The detection protocol for all three events was restricted to periods of NREM sleep.

The Freely Moving Animal (FMA) toolbox[65] was used for slow wave and spindle detection. For slow waves, mPFC and reuniens LFP signals were bandpass filtered between 0.5 to 4 Hz using a FIR filter with a filter order corresponding to 3 cycles of the low frequency cut-off. Tentative slow wave events whose positive peaks were greater than 2.5 standard deviations of the signal and whose difference between positive and negative peaks was greater than 4 standard

deviations were detected. Slow waves were finally defined as periods when consecutive positive-to-negative zero crossings of the signal filtered in 0.5-2 Hz occurred between 0.5 and 2 seconds of each other.

For spindles, mPFC and reuniens LFP signals were bandpassed in the spindle frequency band (7-15 Hz) using finite-impulse-response (FIR) filters from the EEGLAB toolbox [68]. The instantaneous amplitude of the filtered signal was then computed from its Hilbert transform and the results were smoothed using a 300 ms Gaussian window. Potential spindles were detected as periods when this signal crossed 3 standard deviations (SD) above its mean for 0.5-3 s A threshold of 2.5 SD above the mean was set to detect spindle onset and offset. Events that occurred within 0.5 seconds of each other were merged into a single event. Events longer than 0.5 s and shorter than 3 s were defined as spindles. The largest peak in spindle amplitude was defined as the time of the spindle event.

For SWRs, hippocampal LFP signals were bandpassed in the ripple frequency band (150-200 Hz, FIR filter from the EEGLAB toolbox). The root mean square (RMS) of the filtered signal was then computed and the results were smoothed using a 50 ms Gaussian windows. SWRs were defined as periods when the smoothed RMS crossed 4 standard deviations above the median and stayed crossed for at least 30 ms. The largest peak in SWR amplitude was defined as the time of the SWR event.

Phase-amplitude coupling

Computations of phase-amplitude coupling (PAC) were based on methodology published previously in Alizadeh et al.[64], Dehnavi et al.[69] and Staresina et al.[70] Time-frequency

representations (TFRs) of every spindle/slow wave event were obtained using the *mtmconvol* function in the FieldTrip toolbox[71]. Spindle power around the slow wave was estimated using sliding Hanning tapered windows (10 ms steps) with a variable length that included five cycles. To compute coupling, TFRs were then normalized as percentage change from pre-event baseline (-3.5 to -2.5 second before event) for all events. To calculate the modulation of spindle power by slow wave phase, TFR bins around slow waves were averaged across the spindle frequency range and then filtered in the slow wave frequency range. Phase values of this signal were calculated from their Hilbert transform.

Synchronization index and coupling strength

We defined a synchronization index (SI) for each event:

$$SI = \frac{1}{m}\sum_{j=1}^{m} e^{i[\theta_{slow\ wave}(j) - \theta_{spindle}(j)]}$$

where m is the number of time points, $\theta_{slow\ wave}(j)$ represents slow wave phase value at time *j* and $\theta_{spindle}(j)$ represents phase values of spindle power fluctuations at time *j*. Preferred phase was estimated in the interval -0.25 to 0.25s around slow wave peak. The strength of phase-amplitude coupling was estimated from the absolute value of the SI with 1 representing the most consistent phase shift between spindle amplitude and slow wave event. The phase of SI represents the amount of phase shift between the spindle amplitude and slow wave event. Spindle-SWR coupling was computed using a similar procedure. Briefly, the normalized TFRs in the SWR frequency range around each spindle event (baseline defined from -2.5 to -1.5 second before spindle event) were filtered in the spindle frequency range and the SI was defined as the

vector mean of unit vectors, each showing the phase difference between SWR amplitude and slow wave event at different time points around the spindle peak.

Average wavelet transforms

Wavelet transforms of the LFP were calculated using the continuous one-dimensional wavelet transform, estimated by Morse wavelets defined in the *cwt* function, available in the MATLAB wavelet toolbox. Average wavelet transforms around spindle onsets (Figure 2L) were computed using custom-written MATLAB code. First, 5-second LFP epochs, centered on spindle onsets were extracted from the continuous recordings and downsampled to 250 Hz. A filter bank, based on the known epoch length (5 s) and sampling frequency (250 Hz), was created with voices per octave set to 20 and frequency limits set to 0.1 to 50 Hz. Using the filter bank, wavelet transforms of each epoch around a spindle onset were calculated and stored in a 3-dimensional array corresponding to time, frequency, and spindle event. To obtain the magnitude of the signal, the absolute value of the wavelet transform was then computed. To obtain the average wavelet transform of the LFP signals around the spindle event onsets, the mean of the magnitude matrices along the third dimension (spindle events) was calculated.

Spike detection

For spike detection, reuniens LFP signals were bandpass filtered in the 300-8000 Hz range using finite impulse response (FIR) filters from the EEGLAB toolbox. Epochs of ± 250 ms around times when the signal crossed ± 16 SD were considered as artifacts and removed from the analysis. Spikes were detected using UltraMegaSort2000 [72] with a negative threshold of -4SD. During a shadow time of 0.75 ms after the threshold crossing, no new event was detected to avoid

547 multiple threshold crossings of one event. A window of 1.5 ms was considered around each
548 detected spike from 0.6 ms before the threshold crossing time to 0.9 ms after this time.

549 Spike sorting was based on a method described previously in Souza et al.[73]. We first extracted
550 spike features for each channel. The features consisted of peak-to-trough value, trough value
551 and also an index which was set to one for the channel with maximum trough amplitude and
552 zero for the other channels. We used principal component analysis (PCA) to combine 12
553 features (3 features times 4 channels) and selected the two first components. Gaussian
554 distributions were fitted to PCA components with gaussian mixture model (GMM) algorithm.
555 Each distribution was determined as a potential spike cluster. We further limited the
556 distribution by removing spikes with large Mahalanobis distance from the center of the
557 distribution. We removed, combined, and limited the distributions manually by visual
558 inspection of the plots showing PCA components versus each other and the plots showing the
559 features for different channel pairs (Figure 2 – figure supplement 1). For multi-unit analysis,
560 spikes were detected according to threshold crossing and template matching algorithms in
561 Spike2[74]. Briefly, fast signals (~1-3 ms) that exceeded the threshold were first detected as
562 putative spikes and timestamped. Thresholds were manually determined according to the
563 signal-to-noise ratio of spikes in each recording. Next, a temporary spike template was formed
564 according to the shape of the putative spike and a “template width” was estimated (twice the
565 mean difference between the template and the spike that created it). Each new spike was then
566 compared against the template and added to it if the spike’s sample points fell within the
567 template width. The template was modified with the addition of each new spike up to a
568 maximum of eight spikes after which the template was checked against previous templates. If a

match was found, the temporary template was merged with the existing template. Otherwise, a new confirmed template was generated.

Peri-event histograms

To analyze reuniens single-unit activity around the onset of SWRs, peri-event spike histograms (PETHs) were calculated for a 1-second period around each event onset and the results were smoothed with a 10 ms Gaussian window. For comparison, surrogate PETHs were obtained by randomly shuffling SWR events detected within 1 second windows. This procedure was repeated 100 times. True-even PETHs were z-score normalized to the firing rate of surrogate PETHs. Single-units with activity greater than 2 SDs and smaller than -2 SDs in the 150 ms window following SWR onset were considered activated and suppressed, respectively.

Phase-locking analysis

For phase-locking analysis, we calculated spindle phase at the time of single-unit spikes occurring within ± 0.25 s around spindle peak (Figure 2H), slow wave phase at SWR time (Figure 3K) and theta phase at single-unit spike time occurring within ± 0.5 s around theta peak (Figure 4C). First, mPFC and reuniens LFPs were filtered in the frequency band of interest (spindle, slow wave, or theta) and the phase of the filtered signal was extracted from its Hilbert transform. These phase values were used to obtain phase histograms and calculate circular means.

Computational model

Our model represents a minimal neural mass model that describes the network architecture required for generating three key oscillatory activities during NREM: the slow oscillation, spindles, and SWRs. The hippocampal-thalamocortical model represents CA1-CA3 networks,

590 two cortical networks (CX, CX'), and three thalamic networks consisting of mediodorsal nucleus

591 of the thalamus (MD), thalamic reticular nucleus (TRN) and nucleus reuniens (REU). The details

592 of the CA1-CA3, MD-TRN and cortical networks were described previously [30,75,76]. In brief, in this

593 neural mass firing rate model, each of cortical and hippocampal networks consists of one

594 identical group of excitatory and one identical group of inhibitory neurons. V_k^m and

595 N_k^m indicate the membrane potential and the number of type k (either e, excitatory or i,

596 inhibitory) neurons of network m, respectively. The firing rates of hippocampal and cortical

597 neurons as well as the REU neurons are sigmoid functions of the membrane potential of the

598 neurons with the sharpness and threshold of g_k^m , V_k^{*m} respectively:

599 $$r(V_k^m) = r_0 + \frac{r_1}{1 + exp[-(V_k^m - V_k^{*m}) / g_k^m]} \quad , \{m\} \in \{CA3, CA1, CX, CX', REU\} \quad (1)$$

600 where, r_1 = 70 Hz (r_0 = 0.1 Hz) is the maximal (minimum) firing rate. T-type calcium currents is

601 modeled only for MD and TRN neurons by defining a bursting variable, u_m so that these

602 neurons show burst mode in addition to the tonic mode:

603 $$r(V_k^m) = \frac{R_k^T}{1+exp[(V_k^m - V_k^T) / g_k^T]}(exp[L_k u_k]) + \frac{R_k^B}{1+exp[(V_k^m - V_k^B) / g_k^B]}(1 - exp[L_k u_k]) , \quad \{m\} \in \{\mathrm{MD, TRN}\} \quad (2)$$

604 Here g_k^T (g_k^B) , R_k^T (R_k^B), and V_k^T(V_k^B) show the sharpness of the firing rate dependence on the

605 membrane potential , the maximum firing rate, and the threshold potential during tonic (burst)

606 mode. The sharpness of switch between the two modes is controlled by L_k (a positive

607 parameter).

The probability and the strength of connections from neuron k of network m to neuron j of network n are shown by $P_{kj}^{m\text{-}n}$ and $J_{kj}^{m\text{-}n}$ respectively. m and n can be CA1, CA3, CX , MD , TRN or REU. k and j can take e or i (representing excitatory and inhibitory neurons, respectively). For the short-range connections since m and n are equal, only one of them is shown. E-E connections of cortical and hippocampal excitatory neurons are subject to dendritic spike frequency adaptation so that $J_{ee}^{m}/J_{ee}^{n\text{-}m}$ is a sigmoid function of an adaptation variable, c^m with sharpness and threshold of g_c and c^* respectively:

$$J_{ee}^{m}(c) = \frac{J0_{ee}^{m}}{1 + exp[c - c^*) / g_c]} \qquad (3)$$

Here $J0_{ee}^{m}$ is the maximal synaptic strength. The full model is described by 17 rate equations:

$$\frac{dV_e^{CA3}}{dt} = - \frac{V_e^{CA3}}{\tau_e} + N_e^{CA3} P_{ee}^{CA3} J_{ee}^{CA3}\left(c^{CA3}\right) r(V_i^{CA3}) - N_i^{CA3} P_{ie}^{CA3} J_{ie}^{CA3} r\left(V_i^{CA3}\right) \qquad (4)$$

$$\frac{dV_i^{CA3}}{dt} = - \frac{V_i^{CA3}}{\tau_I} + N_e^{CA3} P_{ei}^{CA3} J_{ei}^{CA3} r(V_e^{CA3}) - N_i^{CA3} P_{ii}^{CA3} J_{ii}^{CA3} r(V_i^{CA3}) \qquad (5)$$

$$\frac{dc^{CA3}}{dt} = - \frac{c^{CA3}}{\tau_c} + N_e^{CA3} P_{ee}^{CA3} \Delta c^{CA3} r\left(V_e^{CA3}\right) \qquad (6)$$

$$\frac{dV_e^{CA1}}{dt} = - \frac{V_e^{CA1}}{\tau_e} - N_i^{CA1} P_{ie}^{CA1} J_{ie}^{CA1} r(V_i^{CA1}) + N_e^{CA3} P_{ee}^{CA3\text{-}CA1} J_{ee}^{CA3\text{-}CA1}(c^{CA1}) r(V_e^{CA3})$$

$$+ N_e^{REU} P_{ee}^{REU\text{-}CA1} J_{ee}^{REU\text{-}CA1}(c^{CA1}) r(V_e^{REU}) \qquad (7)$$

$$\frac{dV_i^{CA1}}{dt} = - \frac{V_i^{CA1}}{\tau_I} + N_e^{CA1} P_{ei}^{CA1} J_{ei}^{CA1} r(V_e^{CA1}) + N_e^{CA3} P_{ei}^{CA3\text{-}CA1} J_{ei}^{CA3\text{-}CA1} r(V_e^{CA3}) -$$

$$N_i^{CA1} P_{ii}^{CA1} J_{ii}^{CA1} r(V_i^{CA1}) + N_e^{REU} P_{ei}^{REU\text{-}CA1} J_{ei}^{REU\text{-}CA1} r(V_e^{REU}) \qquad (8)$$

$$\frac{dc^{CA1}}{dt} = - \frac{c^{CA1}}{\tau_c} + N_e^{CA3} P_{ee}^{CA3\text{-}CA1} \Delta c^{CA1} r(V_e^{CA3}) + N_e^{REU} P_{ee}^{REU\text{-}CA1} \Delta c^{CA1} r(V_e^{REU}) \qquad (9)$$

$$\frac{dV_e^{CX}}{dt} = -\frac{V_e^{CX}}{\tau_e} + N_e^{CX} P_{ee}^{CX} J_{ee}^{CX}(c^{CX}) r(V_e^{CX}) - N_i^{CX} P_{ie}^{CX} J_{ie}^{CX} r(V_i^{CX}) + N_e^{'CX} P_{ee}^{CX2\text{-}CX1} J_{ee}^{CX2\text{-}CX1}(c^{CX}) r(V_e^{'CX}) +$$

$$N_e^{REU} P_{ee}^{REU\text{-}CX} J_{ee}^{REU\text{-}CX}(c^{CX}) r(V_e^{REU}) + N_e^{CA1} P_{ee}^{CA1\text{-}CX} J_{ee}^{CA1\text{-}CX}(c^{CX}) r(V_e^{CA1}) \qquad (10)$$

$$\frac{dc^{CX}}{dt} = -\frac{c^{CX}}{\tau_c} + N_e^{CX} P_{ee}^{CX} \Delta c^{CX} r(V_e^{CX}) + N_e^{'CX} P_{ee}^{CX2\text{-}CX1} \Delta c^{CX} r(V_e^{'CX}) + N_e^{REU} P_{ee}^{REU\text{-}CX} \Delta c^{CX} r(V_e^{REU})$$

$$+ N_e^{CA1} P_{ee}^{CA1\text{-}CX} \Delta c^{CX} r(V_e^{CA1}) \qquad (11)$$

$$\frac{dV_i^{CX}}{dt} = -\frac{V_i^{CX}}{\tau_I} - N_i^{CX} P_{ii}^{CX} J_{ii}^{CX} r(V_i^{CX}) + N_e^{CX} P_{ei}^{CX} J_{ei}^{CX} r(V_e^{CX}) + N_e^{'CX} P_{ei}^{CX2\text{-}CX1} J_{ei}^{CX2\text{-}CX1} r(V_e^{'CX}) +$$

$$N_e^{REU} P_{ei}^{REU\text{-}CX} J_{ei}^{REU\text{-}CX} r(V_e^{REU}) + N_e^{CA1} P_{ei}^{CA1\text{-}CX} J_{ei}^{CA1\text{-}CX} r(V_e^{CA1}) \qquad (12)$$

$$\frac{dV_e^{'CX}}{dt} = -\frac{V_e^{'CX}}{\tau_e} - N_I^{'CX} P_{ie}^{'CX} J_{ie}^{'CX} r(V_I^{'CX}) + N_e^{'CX} P_{ee}^{'CX} J_{ee}^{'CX}(c^{'CX}) r(V_e^{'CX}) + N_e^{CX} P_{ee}^{CX1\text{-}CX2} J_{ee}^{CX1\text{-}CX2}(c^{'CX}) r(V_e^{CX}) +$$

$$N_e^{MD} P_{ee}^{'MD\text{-}CX} J_{ee}^{'MD\text{-}CX}(c^{'CX}) r(V_e^{MD}) \qquad (13)$$

$$\frac{dc^{'CX}}{dt} = -\frac{c^{'CX}}{\tau_c} + N_e^{'CX} P_{ee}^{'CX} \Delta c^{'CX} r(V_e^{'CX}) + N_e^{CX} P_{ee}^{CX1\text{-}CX2} \Delta c^{'CX} r(V_e^{CX}) + N_e^{MD} P_{ee}^{'MD\text{-}CX} \Delta c^{'CX} r(V_e^{MD})$$

(14)

$$\frac{dV_I^{'CX}}{dt} = -\frac{V_I^{'CX}}{\tau_I} + N_e^{'CX} P_{ei}^{'CX} J_{ei}^{'CX} r(V_e^{'CX}) - N_I^{'CX} P_{ii}^{'CX} J_{ii}^{'CX} r(V_I^{'CX}) + N_e^{CX} P_{ei}^{CX1\text{-}CX2} J_{ei}^{CX1\text{-}CX2} r(V_e^{CX}) +$$

$$N_e^{MD} P_{ei}^{'MD\text{-}CX} J_{ei}^{'MD\text{-}CX} r(V_e^{MD}) \qquad (15)$$

$$\frac{dV_e^{MD}}{dt} = -\frac{V_e^{MD}}{\tau_{MD}} - \frac{f_e^{max}}{1 + exp[\frac{(u_e + f_e^{th})}{q_e}]} - N_i^{TRN} P_{ie}^{TRN\text{-}MD} J_{ie}^{TRN\text{-}MD} r(V_i^{TRN}) + N_e^{'CX} P_{ee}^{'CX\text{-}MD} J_{ee}^{'CX\text{-}MD} r(V_e^{'CX})$$

(16)

$$\frac{du_e}{dt} = [\frac{1}{\tau_e^u}(b_e - u_e)] \quad \text{if} \quad V_e^{MD} > -0.1 \text{ mV} \quad \text{then} \quad b_e = 0 \quad \text{otherwise} \quad b_e = -200 \text{ mA} \qquad (17)$$

$$\frac{dV_i^{TRN}}{dt} = -\frac{V_i^{TRN}}{\tau_{TRN}} - \frac{f_i^{max}}{1 + exp[\frac{(u_I + f_i^{th})}{q_i}]} - N_i^{TRN} P_{ii}^{TRN} J_{ii}^{TRN} r(V_i^{TRN}) + N_e^{MD} P_{ei}^{MD\text{-}TRN} J_{ei}^{MD\text{-}TRN} r(V_e^{MD}) + N_e^{'CX} P_{ei}^{'CX\text{-}TRN} J_{ei}^{'CX\text{-}TRN} r(V_e^{'CX}) \quad (18)$$

$$\frac{du_i}{dt} = [\frac{1}{\tau_i^u}(b_I - u_i)] \qquad \text{if} \quad V_i^{TRN} > 0 \text{ mV} \quad \text{then} \quad b_I = 0 \quad \text{otherwise} \quad b_i = \text{-}200 \text{ mA} \quad (19)$$

$$\frac{dV_e^{REU}}{dt} = -\frac{V_e^{REU}}{\tau_{REU}} - N_i^{TRN} P_{ie}^{TRN\text{-}REU} J_{ie}^{TRN\text{-}REU} r(V_i^{TRN}) + N_e^{CX} P_{ee}^{CX\text{-}REU} J_{ee}^{CX\text{-}REU} r(V_e^{CX}) + N_e^{CA1} P_{ee}^{CA1\text{-}REU} J_{ee}^{CA1\text{-}REU} r(V_e^{CA1}) \quad (20)$$

The nonlinear equations of the model were solved using the fourth-order Runge–Kutta method with a time step of 1 ms by MATLAB R2017b software.

Quantification and statistical analysis

Statistical analyses were performed using the MATLAB Statistics and Machine Learning Toolbox (Mathworks Inc., Natick, MA, USA). Phase analysis was performed using the circular statistics tool box developed by Berens [77]. The Rayleigh test was performed to determine the uniformity in the phase preference of events. The Watson-Williams test was used to test the inequality of phases. Polar plots showing phases, and mean phases were plotted using MATLAB.

Intracellular data was analyzed using JMP 5.01 software. Normality was assessed by normal quantile plots and by the Shapiro-Wilk test. Homogeneity of variance was assessed by Levene's test. Confidence intervals were set at 95% ($p<0.05$). ANOVA was used when data was normally distributed and variance homogeneous, Welch ANOVA when variance was non-homogeneous. To determine group differences in normally distributed data, Tukey's range test was used.

Otherwise, differences were assessed by non-parametric testing (van der Waerden test). Standard deviations are reported as SD and the mean absolute deviation is reported as MAD.

Data and code availability

Further information and requests for resources and reagents should be directed to and will be fulfilled by the Lead Contact, Igor Timofeev (igor.timofeev@fmed.ulaval.ca). Original electrophysiological recordings have been deposited at Mendeley Data and are publicly available as of the date of publication.

The following data sets were generated

Basha, Diellor; Timofeev, Igor (2022), "Natural sleep electrophysiology: mPFC, thalamus, hippocampus", Mendeley Data, V2, doi: 10.17632/4x27jjp9mv.2[58]. In the public domain at Mendeley Data, https://data.mendeley.com/datasets/4x27jjp9mv/2.

MATLAB code generated for this study is available at https://github.com/DiellorBasha/MATLAB_for_Electrophysiology and https://github.com/azarmehri/brain-network-interactions.

Tetrodes and stainless-steel electrodes manufactured in-house for this study are available from the lead contact with a completed materials transfer agreement. This study did not generate new unique reagents. Any additional information required to reanalyze the data reported in this paper is available from the lead contact upon request.

676 **Key Resources Table**

Key Resources Table				
Reagent type (species) or resource	**Designation**	**Source or reference**	**Identifiers**	**Additional information**
strain, cat (males and females)	Cat	Marshall BioResources	Marshall Cat, domestic short-hair	
software, algorithm	MATLAB	This paper	https://github.com/DiellorBasha/MATLAB_for_Electrophysiology	
software, algorithm	MATLAB	This paper	https://github.com/azarmehri/brain-network-interactions	
software, algorithm	Spike2 9.14	Cambridge Electronic Design	N/A	
software, algorithm	FieldTrip	Oostenveld et al., 2011	N/A	

software, algorithm	CircStat	Berens, P. 2009	N/A	
software, algorithm	UltraMegaSort2000 (ums2k)	Neurophysics Lab, UCSD	https://neurophysics.ucsd.edu/software.php	
software, algorithm	Freely Moving Animal (FMA) Toolbox		https://fmatoolbox.sourceforge.net/	
software, algorithm	LabChart 8	ADI Instruments	N/A	
software, algorithm	IgorPro 7	Wavemetrics	N/A	
software, algorithm	Canvas 11	ACDSee	N/A	
chemical compound, drug	DAPI	Invitrogen	D3571	
other, equipment	AM 3000 amplifiers	A-M systems	N/A	
other, equipment	PowerLab 35 Series Data Acquisition	ADI instruments	N/A	
other, equipment	Neurodata IR-283 amplifiers	Cygnus Technology	N/A	
other, equipment	Tetrodes	Custom, This paper	N/A	

References

1. Siapas, A.G., and Wilson, M.A. (1998). Coordinated interactions between hippocampal ripples and cortical spindles during slow-wave sleep. Neuron *21*, 1123-1128. 10.1016/s0896-6273(00)80629-7.

682 2. Isomura, Y., Sirota, A., Özen, S., Montgomery, S., Mizuseki, K., Henze, D.A., and Buzsáki,
683 G. (2006). Integration and Segregation of Activity in Entorhinal-Hippocampal Subregions
684 by Neocortical Slow Oscillations. Neuron *52*, 871-882. 10.1016/j.neuron.2006.10.023.
685 3. Chauvette, S., Seigneur, J., and Timofeev, I. (2012). Sleep Oscillations in the
686 Thalamocortical System Induce Long-Term Neuronal Plasticity. Neuron *75*, 1105-1113.
687 10.1016/j.neuron.2012.08.034.
688 4. Diekelmann, S., and Born, J. (2010). The memory function of sleep. Nature reviews.
689 Neuroscience *11*, 114-126. 10.1038/nrn2762.
690 5. Maingret, N., Girardeau, G., Todorova, R., Goutierre, M., and Zugaro, M. (2016).
691 Hippocampo-cortical coupling mediates memory consolidation during sleep. Nature
692 Neuroscience *19*. 10.1038/nn.4304.
693 6. Latchoumane, C.-F.V., Ngo, H.-V.V., Born, J., and Shin, H.-S. (2017). Thalamic Spindles
694 Promote Memory Formation during Sleep through Triple Phase-Locking of Cortical,
695 Thalamic, and Hippocampal Rhythms. Neuron *95*, 424-435.e426.
696 10.1016/j.neuron.2017.06.025.
697 7. Swanson, L.W. (1981). A direct projection from Ammon's horn to prefrontal cortex in
698 the rat. Brain research *217*, 150-154. 10.1016/0006-8993(81)90192-x.
699 8. Jay, T.M., and Witter, M.P. (1991). Distribution of hippocampal CA1 and subicular
700 efferents in the prefrontal cortex of the rat studied by means of anterograde transport
701 of Phaseolus vulgaris-leucoagglutinin. J Comp Neurol *313*, 574-586.
702 10.1002/cne.903130404.
703 9. Irle, E., and Markowitsch, H.J. (1982). Widespread cortical projections of the
704 hippocampal formation in the cat. Neuroscience *7*, 2637-2647. 10.1016/0306-
705 4522(82)90088-4.
706 10. Cavada, C., Llamas, A., and Reinoso-Suárez, F. (1983). Allocortical afferent connections
707 of the prefrontal cortex in the cat. Brain research *260*, 117-120. 10.1016/0006-
708 8993(83)90769-2.
709 11. Goldman-Rakic, P.S., Selemon, L.D., and Schwartz, M.L. (1984). Dual pathways
710 connecting the dorsolateral prefrontal cortex with the hippocampal formation and
711 parahippocampal cortex in the rhesus monkey. Neuroscience *12*, 719-743.
712 10.1016/0306-4522(84)90166-0.
713 12. Rajasethupathy, P., Sankaran, S., Marshel, J.H., Kim, C.K., Ferenczi, E., Lee, S.Y., Berndt,
714 A., Ramakrishnan, C., Jaffe, A., Lo, M., et al. (2015). Projections from neocortex mediate
715 top-down control of memory retrieval. Nature *526*, 653-659. 10.1038/nature15389.
716 13. Beckstead, R.M. (1979). An autoradiographic examination of corticocortical and
717 subcortical projections of the mediodorsal-projection (prefrontal) cortex in the rat. J
718 Comp Neurol *184*, 43-62. 10.1002/cne.901840104.
719 14. Room, P., Russchen, F.T., Groenewegen, H.J., and Lohman, A.H. (1985). Efferent
720 connections of the prelimbic (area 32) and the infralimbic (area 25) cortices: an
721 anterograde tracing study in the cat. J Comp Neurol *242*, 40-55.
722 10.1002/cne.902420104.
723 15. Reep, R.L., Corwin, J.V., Hashimoto, A., and Watson, R.T. (1987). Efferent connections of
724 the rostral portion of medial agranular cortex in rats. Brain Res Bull *19*, 203-221.
725 10.1016/0361-9230(87)90086-4.

16. Takagishi, M., and Chiba, T. (1991). Efferent projections of the infralimbic (area 25) region of the medial prefrontal cortex in the rat: an anterograde tracer PHA-L study. Brain research *566*, 26-39. 10.1016/0006-8993(91)91677-s.
17. Vertes, R.P., Hoover, W.B., Szigeti-Buck, K., and Leranth, C. (2007). Nucleus reuniens of the midline thalamus: Link between the medial prefrontal cortex and the hippocampus. Brain Research Bulletin *71*, 601-609. 10.1016/j.brainresbull.2006.12.002.
18. Herkenham, M. (1978). The connections of the nucleus reuniens thalami: Evidence for a direct thalamo-hippocampal pathway in the rat. The Journal of Comparative Neurology *177*, 589-609. 10.1002/cne.901770405.
19. Robertson, R.T., and Kaitz, S.S. (1981). Thalamic connections with limbic cortex. I. Thalamocortical projections. J Comp Neurol *195*, 501-525. 10.1002/cne.901950308.
20. Vertes, R.P., Hoover, W.B., Do Valle, A.C., Sherman, A., and Rodriguez, J.J. (2006). Efferent projections of reuniens and rhomboid nuclei of the thalamus in the rat. The Journal of Comparative Neurology *499*, 768-796. 10.1002/cne.21135.
21. McKenna, J.T., and Vertes, R.P. (2004). Afferent projections to nucleus reuniens of the thalamus. J Comp Neurol *480*, 115-142. 10.1002/cne.20342.
22. Ohtake, T., and Yamada, H. (1989). Efferent connections of the nucleus reuniens and the rhomboid nucleus in the rat: an anterograde PHA-L tracing study. Neurosci Res *6*, 556-568. 10.1016/0168-0102(89)90044-8.
23. Ramanathan, K.R., Ressler, R.L., Jin, J., and Maren, S. (2018). Nucleus Reuniens Is Required for Encoding and Retrieving Precise, Hippocampal-Dependent Contextual Fear Memories in Rats. J Neurosci *38*, 9925-9933. 10.1523/jneurosci.1429-18.2018.
24. Xu, W., and Sudhof, T.C. (2013). A neural circuit for memory specificity and generalization. Science *339*, 1290-1295. 10.1126/science.1229534.
25. Ramanathan, K.R., and Maren, S. (2019). Nucleus reuniens mediates the extinction of contextual fear conditioning. Behav Brain Res *374*, 112114. 10.1016/j.bbr.2019.112114.
26. Di Prisco, G.V., and Vertes, R.P. (2006). Excitatory actions of the ventral midline thalamus (rhomboid/reuniens) on the medial prefrontal cortex in the rat. Synapse *60*, 45-55. 10.1002/syn.20271.
27. Frankland, P.W., and Bontempi, B. (2005). The organization of recent and remote memories. Nature Reviews Neuroscience *6*, 119. 10.1038/nrn1607.
28. Timofeev, I., and Chauvette, S. (2019). Chapter 29 - Sleep-Wake and Cortical Synaptic Plasticity. In Handbook of Behavioral Neuroscience, H.C. Dringenberg, ed. (Elsevier), pp. 443-454. https://doi.org/10.1016/B978-0-12-813743-7.00029-3.
29. Chang, H.T. (1953). Cortical response to activity of callosal neurons. J Neurophysiol *16*, 117-131. 10.1152/jn.1953.16.2.117.
30. Azimi, A., Alizadeh, Z., and Ghorbani, M. (2021). The essential role of hippocampo-cortical connections in temporal coordination of spindles and ripples. Neuroimage *243*, 118485. 10.1016/j.neuroimage.2021.118485.
31. Bontempi, B., Laurent-Demir, C., Destrade, C., and Jaffard, R. (1999). Time-dependent reorganization of brain circuitry underlying long-term memory storage. Nature *400*, 671-675. 10.1038/23270.

32. Siapas, A.G., Lubenov, E.V., and Wilson, M.A. (2005). Prefrontal Phase Locking to Hippocampal Theta Oscillations. Neuron *46*, 141-151. https://doi.org/10.1016/j.neuron.2005.02.028.
33. Wilson, M.A., and McNaughton, B.L. (1994). Reactivation of hippocampal ensemble memories during sleep. Science *265*, 676-679.
34. Degenetais, E., Thierry, A.M., Glowinski, J., and Gioanni, Y. (2003). Synaptic influence of hippocampus on pyramidal cells of the rat prefrontal cortex: an in vivo intracellular recording study. Cerebral cortex (New York, N.Y. : 1991) *13*, 782-792.
35. Gigg, J., Tan, A.M., and Finch, D.M. (1994). Glutamatergic hippocampal formation projections to prefrontal cortex in the rat are regulated by GABAergic inhibition and show convergence with glutamatergic projections from the limbic thalamus. Hippocampus *4*, 189-198. 10.1002/hipo.450040209.
36. Williams, G.V., and Goldman-Rakic, P.S. (1995). Modulation of memory fields by dopamine D1 receptors in prefrontal cortex. Nature *376*, 572-575. 10.1038/376572a0.
37. Floresco, S.B., and Grace, A.A. (2003). Gating of hippocampal-evoked activity in prefrontal cortical neurons by inputs from the mediodorsal thalamus and ventral tegmental area. J Neurosci *23*, 3930-3943. 10.1523/JNEUROSCI.23-09-03930.2003.
38. Gioanni, Y., Rougeot, C., Clarke, P.B., Lepouse, C., Thierry, A.M., and Vidal, C. (1999). Nicotinic receptors in the rat prefrontal cortex: increase in glutamate release and facilitation of mediodorsal thalamo-cortical transmission. The European journal of neuroscience *11*, 18-30. 10.1046/j.1460-9568.1999.00403.x.
39. Robbins, T.W. (2005). Chemistry of the mind: neurochemical modulation of prefrontal cortical function. J Comp Neurol *493*, 140-146. 10.1002/cne.20717.
40. Mansvelder, H.D., Mertz, M., and Role, L.W. (2009). Nicotinic modulation of synaptic transmission and plasticity in cortico-limbic circuits. Semin Cell Dev Biol *20*, 432-440. 10.1016/j.semcdb.2009.01.007.
41. Jay, T.M., Thierry, A.M., Wiklund, L., and Glowinski, J. (1992). Excitatory Amino Acid Pathway from the Hippocampus to the Prefrontal Cortex. Contribution of AMPA Receptors in Hippocampo-prefrontal Cortex Transmission. The European journal of neuroscience *4*, 1285-1295. 10.1111/j.1460-9568.1992.tb00154.x.
42. Contreras, D., Timofeev, I., and Steriade, M. (1996). Mechanisms of long-lasting hyperpolarizations underlying slow sleep oscillations in cat corticothalamic networks. J Physiol *494 (Pt 1)*, 251-264.
43. Fuentealba, P., Crochet, S., Timofeev, I., and Steriade, M. (2004). Synaptic interactions between thalamic and cortical inputs onto cortical neurons in vivo. J Neurophysiol *91*, 1990-1998. 10.1152/jn.01105.2003.
44. Tierney, P.L., Dégenètais, E., Thierry, A.M., Glowinski, J., and Gioanni, Y. (2004). Influence of the hippocampus on interneurons of the rat prefrontal cortex. The European journal of neuroscience *20*, 514-524. 10.1111/j.1460-9568.2004.03501.x.
45. Gigg, J., Tan, A.M., and Finch, D.M. (1992). Glutamatergic excitatory responses of anterior cingulate neurons to stimulation of the mediodorsal thalamus and their regulation by GABA: an in vivo iontophoretic study. Cerebral cortex (New York, N.Y. : 1991) *2*, 477-484. 10.1093/cercor/2.6.477.

811 46. Hur, E.E., and Zaborszky, L. (2005). Vglut2 afferents to the medial prefrontal and primary
812 somatosensory cortices: a combined retrograde tracing in situ hybridization study
813 [corrected]. J Comp Neurol *483*, 351-373. 10.1002/cne.20444.
814 47. Pirot, S., Glowinski, J., and Thierry, A.M. (1995). Excitatory responses evoked in
815 prefrontal cortex by mediodorsal thalamic nucleus stimulation: influence of anaesthesia.
816 Eur J Pharmacol *285*, 45-54. 10.1016/0014-2999(95)00377-w.
817 48. Ferraris, M., Ghestem, A., Vicente, A.F., Nallet-Khosrofian, L., Bernard, C., and Quilichini,
818 P.P. (2018). The Nucleus Reuniens Controls Long-Range Hippocampo-Prefrontal Gamma
819 Synchronization during Slow Oscillations. The Journal of neuroscience : the official
820 journal of the Society for Neuroscience *38*, 3026. 10.1523/JNEUROSCI.3058-17.2018.
821 49. Bertram, E.H., and Zhang, D.X. (1999). Thalamic excitation of hippocampal CA1 neurons:
822 a comparison with the effects of CA3 stimulation. Neuroscience *92*, 15-26.
823 10.1016/S0306-4522(98)00712-X.
824 50. Dolleman-Van der Weel, M.J., Lopes da Silva, F.H., and Witter, M.P. (1997). Nucleus
825 reuniens thalami modulates activity in hippocampal field CA1 through excitatory and
826 inhibitory mechanisms. J Neurosci *17*, 5640-5650.
827 51. Bazhenov, M., Timofeev, I., Steriade, M., and Sejnowski, T.J. (1999). Self-sustained
828 rhythmic activity in the thalamic reticular nucleus mediated by depolarizing GABAA
829 receptor potentials. Nat Neurosci *2*, 168-174. 10.1038/5729.
830 52. Steriade, M., Domich, L., Oakson, G., and Deschenes, M. (1987). The deafferented
831 reticular thalamic nucleus generates spindle rhythmicity. J Neurophysiol *57*, 260-273.
832 10.1152/jn.1987.57.1.260.
833 53. Contreras, D., and Steriade, M. (1996). Spindle oscillation in cats: the role of
834 corticothalamic feedback in a thalamically generated rhythm. J Physiol *490 (Pt 1)*, 159-
835 179. 10.1113/jphysiol.1996.sp021133.
836 54. Bonjean, M., Baker, T., Lemieux, M., Timofeev, I., Sejnowski, T., and Bazhenov, M.
837 (2011). Corticothalamic feedback controls sleep spindle duration in vivo. J Neurosci *31*,
838 9124-9134. 10.1523/JNEUROSCI.0077-11.2011.
839 55. Groh, A., Bokor, H., Mease, R.A., Plattner, V.M., Hangya, B., Stroh, A., Deschenes, M.,
840 and Acsády, L. (2014). Convergence of Cortical and Sensory Driver Inputs on Single
841 Thalamocortical Cells. Cerebral Cortex *24*, 3167-3179. 10.1093/cercor/bht173.
842 56. Sheroziya, M., and Timofeev, I. (2014). Global intracellular slow-wave dynamics of the
843 thalamocortical system. J Neurosci *34*, 8875-8893. 10.1523/jneurosci.4460-13.2014.
844 57. Cavdar, S., Onat, F.Y., Cakmak, Y.O., Yananli, H.R., Gulcebi, M., and Aker, R. (2008). The
845 pathways connecting the hippocampal formation, the thalamic reuniens nucleus and the
846 thalamic reticular nucleus in the rat. Journal of anatomy *212*, 249-256. 10.1111/j.1469-
847 7580.2008.00858.x.
848 58. Basha, D., and Timofeev, I. (2022). Natural sleep electrophysiology: mPFC, thalamus,
849 hippocampus. Mendeley Data.
850 59. Timofeev, I., Grenier, F., and Steriade, M. (2001). Disfacilitation and active inhibition in
851 the neocortex during the natural sleep-wake cycle: an intracellular study. Proc Natl Acad
852 Sci U S A *98*, 1924-1929. 10.1073/pnas.041430398.

60. Chauvette, S., Crochet, S., Volgushev, M., and Timofeev, I. (2011). Properties of Slow Oscillation during Slow-Wave Sleep and Anesthesia in Cats. The Journal of Neuroscience *31*, 14998-15008. 10.1523/jneurosci.2339-11.2011.
61. Reinoso-Suárez, F. (1961). Topographischer Hirnatlas der Katze für experimental-physiologische Untersuchungen (Merck).
62. Lipski, J. (1981). Antidromic activation of neurones as an analytic tool in the study of the central nervous system. Journal of neuroscience methods *4*, 1-32. 10.1016/0165-0270(81)90015-7.
63. Costa-Miserachs, D., Portell-Cortés, I., Torras-Garcia, M., and Morgado-Bernal, I. (2003). Automated sleep staging in rat with a standard spreadsheet. Journal of neuroscience methods *130*, 93-101. 10.1016/s0165-0270(03)00229-2.
64. Alizadeh, Z., Azimi, A., and Ghorbani, M. (2022). Enhancement of hippocampal-thalamocortical temporal coordination during slow-frequency long-duration anterior thalamic spindles. J Neurosci. 10.1523/JNEUROSCI.2515-21.2022.
65. Zugaro, M., Todorova, R., Girardeau, G., Cei, A., and El Kanbi, K. (2022). FMAToolbox.
66. Klinzing, J.G., Mölle, M., Weber, F., Supp, G., Hipp, J.F., Engel, A.K., and Born, J. (2016). Spindle activity phase-locked to sleep slow oscillations. Neuroimage *134*, 607-616. 10.1016/j.neuroimage.2016.04.031.
67. Levenstein, D., Buzsáki, G., and Rinzel, J. (2019). NREM sleep in the rodent neocortex and hippocampus reflects excitable dynamics. Nature communications *10*, 2478. 10.1038/s41467-019-10327-5.
68. Delorme, A., and Makeig, S. (2004). EEGLAB: an open source toolbox for analysis of single-trial EEG dynamics including independent component analysis. Journal of neuroscience methods *134*, 9-21. 10.1016/j.jneumeth.2003.10.009.
69. Dehnavi, F., Koo-Poeggel, P.C., Ghorbani, M., and Marshall, L. (2021). Spontaneous slow oscillation-slow spindle features predict induced overnight memory retention. Sleep *44*. 10.1093/sleep/zsab127.
70. Staresina, B.P., Bergmann, T.O., Bonnefond, M., van der Meij, R., Jensen, O., Deuker, L., Elger, C.E., Axmacher, N., and Fell, J. (2015). Hierarchical nesting of slow oscillations, spindles and ripples in the human hippocampus during sleep. Nat Neurosci *18*, 1679-1686. 10.1038/nn.4119.
71. Oostenveld, R., Fries, P., Maris, E., and Schoffelen, J.M. (2011). FieldTrip: Open source software for advanced analysis of MEG, EEG, and invasive electrophysiological data. Comput Intell Neurosci *2011*, 156869. 10.1155/2011/156869.
72. Fee, M.S., Mitra, P.P., and Kleinfeld, D. (1996). Automatic sorting of multiple unit neuronal signals in the presence of anisotropic and non-Gaussian variability. Journal of neuroscience methods *69*, 175-188. 10.1016/S0165-0270(96)00050-7.
73. Souza, B.C., Lopes-Dos-Santos, V., Bacelo, J., and Tort, A.B.L. (2019). Spike sorting with Gaussian mixture models. Sci Rep *9*, 3627. 10.1038/s41598-019-39986-6.
74. CED (2021). Spike2 Version 10 fo Windows: Spike Sorting. Cambridge Electronic Design.
75. Ghorbani, M., Mehta, M., Bruinsma, R., and Levine, A.J. (2012). Nonlinear-dynamics theory of up-down transitions in neocortical neural networks. Phys Rev E Stat Nonlin Soft Matter Phys *85*, 021908. 10.1103/PhysRevE.85.021908.

76. Hashemi, N.S., Dehnavi, F., Moghimi, S., and Ghorbani, M. (2019). Slow spindles are associated with cortical high frequency activity. Neuroimage *189*, 71-84. 10.1016/j.neuroimage.2019.01.012.
77. Berens, P. (2009). CircStat: A Matlab Toolbox for Circular Statistics. Journal of Statistical Software *31*.

Figures

Figure 1 Differential synaptic responses of mPFC neurons to hippocampal and reuniens stimulation

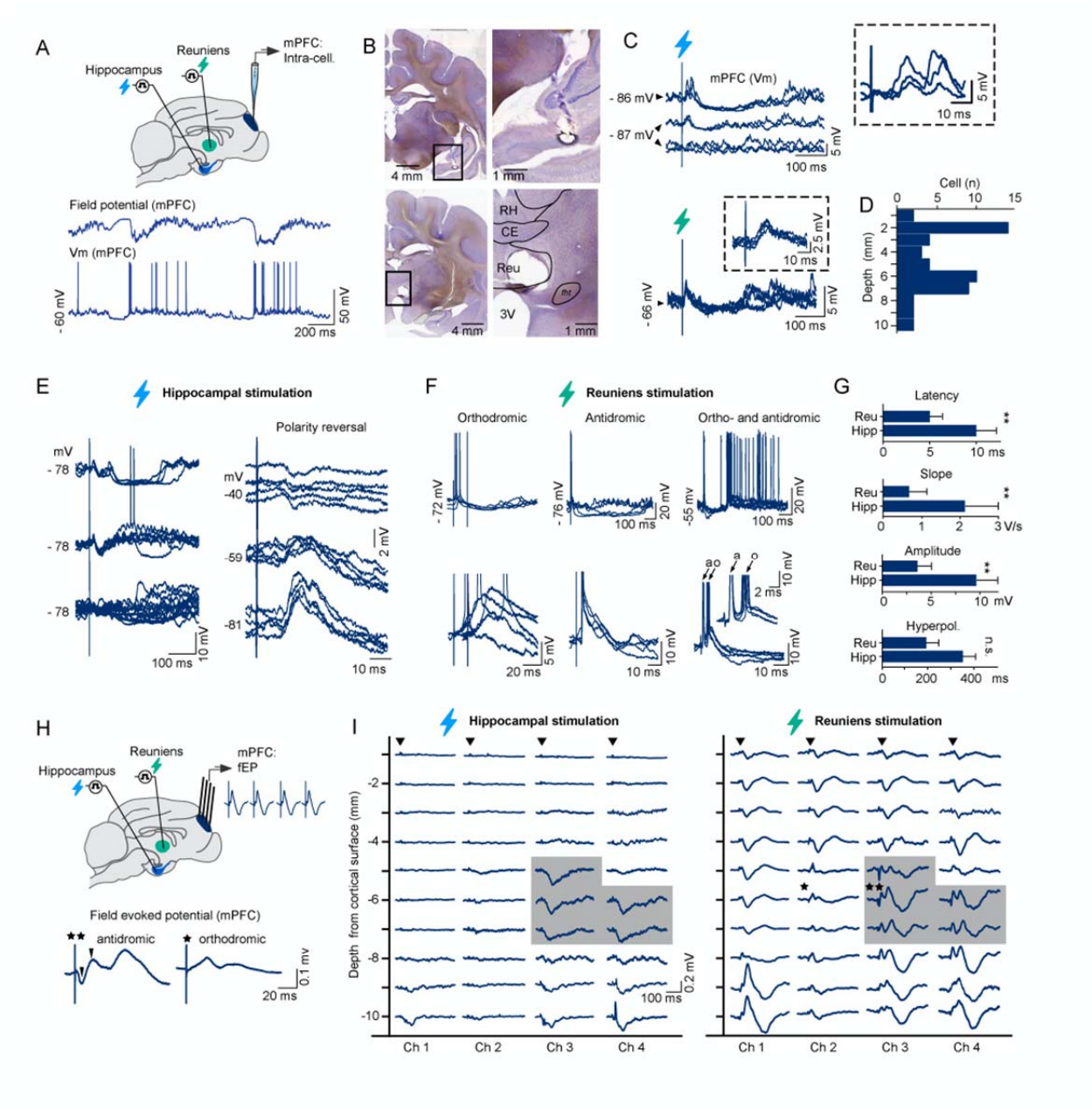

907 A. Schematic of experimental setup: intracellular recordings of the mPFC were
908 obtained in vivo during targeted stimulation of the hippocampus and reuniens (top).
909 Representative segment of intracellular recordings of the mPFC and proximal
910 prefrontal LFP recorded in vivo during anesthesia (bottom).

911 B. Electrolytic lesions at stimulation sites in the ventral hippocampus (top) and midline
912 thalamus (bottom) in Nissl-stained coronal sections.

913 C. mPFC synaptic responses to hippocampal stimulation (top) and reuniens stimulation
914 (bottom), recorded from same neuron, 5.2 mm ventral from the cortical surface.
915 Note, variable, complex responses to hippocampal stimulation (top) and rapid,
916 consistent responses to reuniens stimulation (bottom).

917 D. Location of recorded cells, estimated according to the dorsoventral position of the
918 recording pipette with respect to the cortical surface.

919 E. Heterogeneous postsynaptic potential responses of a single mPFC neuron to
920 consecutive hippocampal stimulation (left): early double depolarizing response
921 (top), early single response (middle), and no response (bottom). Reversal of early
922 response with progressive depolarization (right), indicates involvement of $GABA_A$-
923 mediated inhibition (n=5 pulses at each voltage).

924 F. Intracellular responses to single pulse stimulation of the reuniens nucleus were
925 orthodromic (left, n=17 neurons), antidromic (middle, n=2 neurons) or both
926 orthodromic and antidromic (right, n=1 neuron), consistent with bidirectional

927 connectivity between the reuniens and the mPFC. Jitter in response latency
928 characterized orthodromic spikes (bottom, left), compared to the consistent timing
929 of antidromic spikes (bottom, middle) that were further confirmed with collision
930 tests (not shown).

931 G. Population data (n=49 neurons from 15 animals, mean ± SD), depicting the response
932 properties of mPFC neurons to hippocampal and reuniens stimulation: response
933 latency (6.05±3.6 ms and 9.95±4.6 ms for reuniens and hippocampal stimulation,
934 respectively, t-test, $p<0.01$), response amplitude (3.1±2.0 mV and 8.4±4.1 mV for
935 reuniens and hippocampal stimulation, respectively, t-test, $p<0.01$), slope of the
936 early postsynaptic potential (1.9±0.9 V/s and 0.56±0.27 V/s for reuniens and
937 hippocampal stimulation, respectively, t-test, $p<0.01$) and duration of the late,
938 hyperpolarizing component ($p=0.2$, t-test).

939 H. Schematic of experimental setup illustrating targeted stimulation of the
940 hippocampus and reuniens and field responses recorded from the mPFC at 1 mm
941 intervals along the medial wall of the pericruciate, prefrontal cortex (top). Evidence
942 for antidromic field responses elicited by reuniens stimulation: short-latency, depth-
943 negative events (bottom, left) compared to orthodromic responses lacking this
944 event (bottom, right).

945 I. Topography of mPFC responses to hippocampal and reuniens stimulation.
946 Stimulation of the reuniens evoked field responses in a wider prefrontal territory
947 than hippocampal stimulation. Traces show the average mPFC field response to 10

948 pulses (0.2 ms, 0.3-1.5 mA at 1 Hz). Regions where hippocampal stimulation elicited

949 responses overlapped with regions where reuniens stimulation elicited antidromic

950 responses (grey shading, stars indicate traces expanded in Figure 1H, bottom).

951 Data are presented as mean ± SD; *p < 0.05, **p <0.01, ***p<0.001 (paired t-tests). *Reu -*

952 *reuniens, RH – rhomboid, CE – central, pars medialis, fht – hypothalamic-tegmental fasciculus*

953

954

Figure 2 Reuniens activity and hippocampal SWRs precede the onset of mPFC spindles

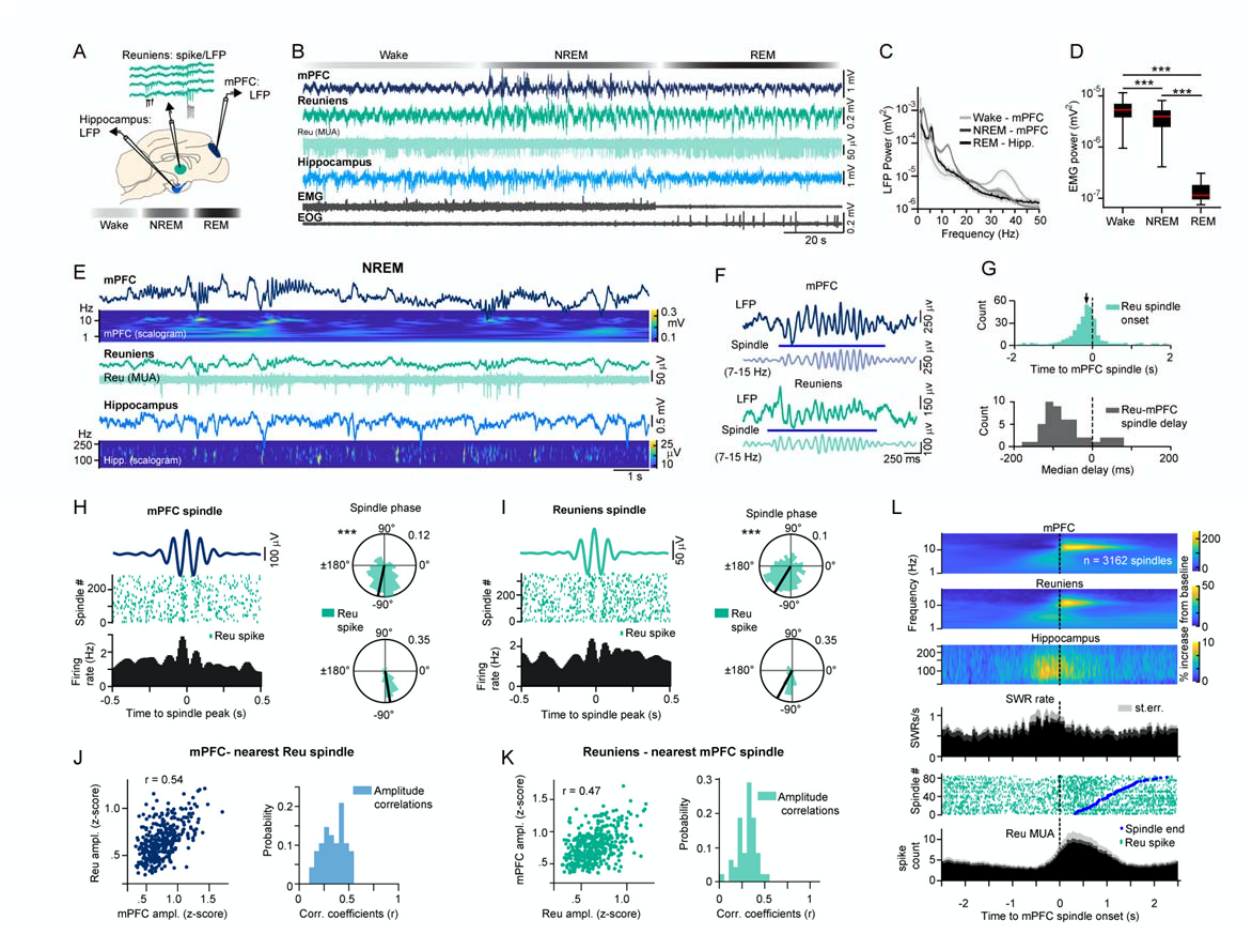

A. Schematic of experimental setup illustrating LFP recordings of the hippocampus and mPFC and targeted spike/LFP recordings of the reuniens during natural sleep.

B. A segment of LFP recordings of the mPFC, reuniens and hippocampus during wake, NREM and REM states. For simplicity, we have chosen a segment with wake followed by unusually short NREM, followed by REM. Sleep/wake states were detected according to mPFC delta (1-4 Hz) power, mPFC signal amplitude and nuchal muscle activity (EMG).

963 C. The average power spectrum of LFP recordings in detected states, showing high gamma
964 power in the mPFC during wake, high delta, and spindle power in the mPFC during
965 NREM and high theta power in the hippocampus during REM (n=52 recording sessions
966 from 4 animals).
967 D. Muscle activity in detected wake, NREM and REM states. The red line in boxplot
968 indicates the median, box limits represent the first and third quartile and whiskers
969 indicate data range. ***$p<0.001$; *post-hoc* Tukey test after one-way ANOVA, n=52
970 recording sessions.
971 E. Representative segment of LFP recordings during NREM with corresponding wavelet
972 transforms of the signal, showing the correlated activity of mPFC slow waves, spindles,
973 hippocampal SWRs (top and bottom) and reuniens multi-unit activity (middle). The
974 frequency axes for wavelet transforms are plotted in logarithmic scale.

975 F. Representative example of overlapping reuniens and mPFC spindles. Blue lines indicate
976 automatically detected spindles in reuniens and mPFC LFPs.

977 G. The relative onset of reuniens spindles with respect to the onset of mPFC spindles in 100
978 ms bins (top). The black arrow indicates the median delay time (median ± MAD = -
979 0.147±0.556s, Wilcoxon signed rank test, $p = 6.13 \times 10^{-15}$, n=346). The distribution of
980 median delay times between each reuniens-mPFC spindle pair for each recording (n=49)
981 in 20 ms bins (bottom, median = -0.083 s, n=49 sessions).

982 H. Reuniens single-unit activity relative to the phase of mPFC spindle cycles, aligned to
983 mPFC spindle peaks. The average prefrontal LFP during spindles, filtered in the spindle

984 frequency range (top left). Spike raster and the associated peri-event histogram of a
985 reuniens single-unit during the above mPFC spindle (bottom left, 10 ms bins). Phase-
986 locking of the same reuniens single-unit to mPFC spindle cycles (top right, n=351 phases,
987 $p = 9.120 \times 10^{-29}$, Rayleigh test) and the mean phase preference of all significantly
988 modulated reuniens single-units (bottom right, n= 24/49 single-units, mean ± SD = -
989 80.87 ± 41.64°, $p = 2.942 \times 10^{-7}$, Rayleigh test).

990 I. Reuniens single-unit activity relative to the phase of reuniens spindle cycles. Same
991 analysis as in H but referenced to reuniens spindles in one session (n=451 phases, p =
992 8.048×10^{-18}, Rayleigh test) and population data (n= 29/49 single-units, mean ± SD = -
993 118.25 ± 47.72°, $p = 1.047 \times 10^{-6}$, Rayleigh test). Polar histograms indicate the
994 normalized count of LFP phases at spike time. The black line indicates the mean phase
995 angle of the associated histogram. Spikes occurred at earlier phases referenced to
996 reuniens spindles compared to mPFC spindles (p = 0.010, Watson-Williams test).

997 J. The amplitude of spindles detected in the mPFC versus the amplitude of the nearest
998 reuniens spindle in one recording session (top, n=343 spindles, r=0.54, $p = 3.22 \times 10^{-27}$,
999 Pearson correlation) and the value of coefficients (r) in mPFC-reuniens amplitude
1000 correlations for all sessions (bottom, n=48 sessions with at least 50 spindles).

1001 K. The amplitude of spindles detected in the reuniens versus the amplitude of the nearest
1002 mPFC spindle in one recording session (top, n=428 spindles, r=0.47, $p = 8.61 \times 10^{-25}$,
1003 Pearson correlation) and the value of coefficients (r) for reuniens-mPFC amplitude
1004 correlations for all sessions (n= 48 sessions with at least 50 spindles).

1005 L. The average change in LFP power during mPFC spindles (n=3162) relative to baseline,
1006 referenced to spindle onset, showing increased hippocampal ripple power, and
1007 increased reuniens spindle power prior to the onset of spindles in the mPFC (top).
1008 Histogram of SWR rate in the same time window, referenced to the onset of the same
1009 mPFC spindles as above (middle). Compared to shuffled data, SWR rate was significantly
1010 higher in the 250 ms window prior to the onset of mPFC spindles (t-test, $p<0.05$). Raster
1011 of reuniens multi-unit activity for a single recording session (n=86 spindles) and the
1012 population peri-event histogram (n=3162 spindles), referenced to the onset of mPFC
1013 spindles.

1014 See also Figure 2 -figure supplement 1 for unit detection.

1015

1016

Figure 3 Slow wave-spindle and slow wave-SWR coupling in the mPFC-reuniens-hippocampal network

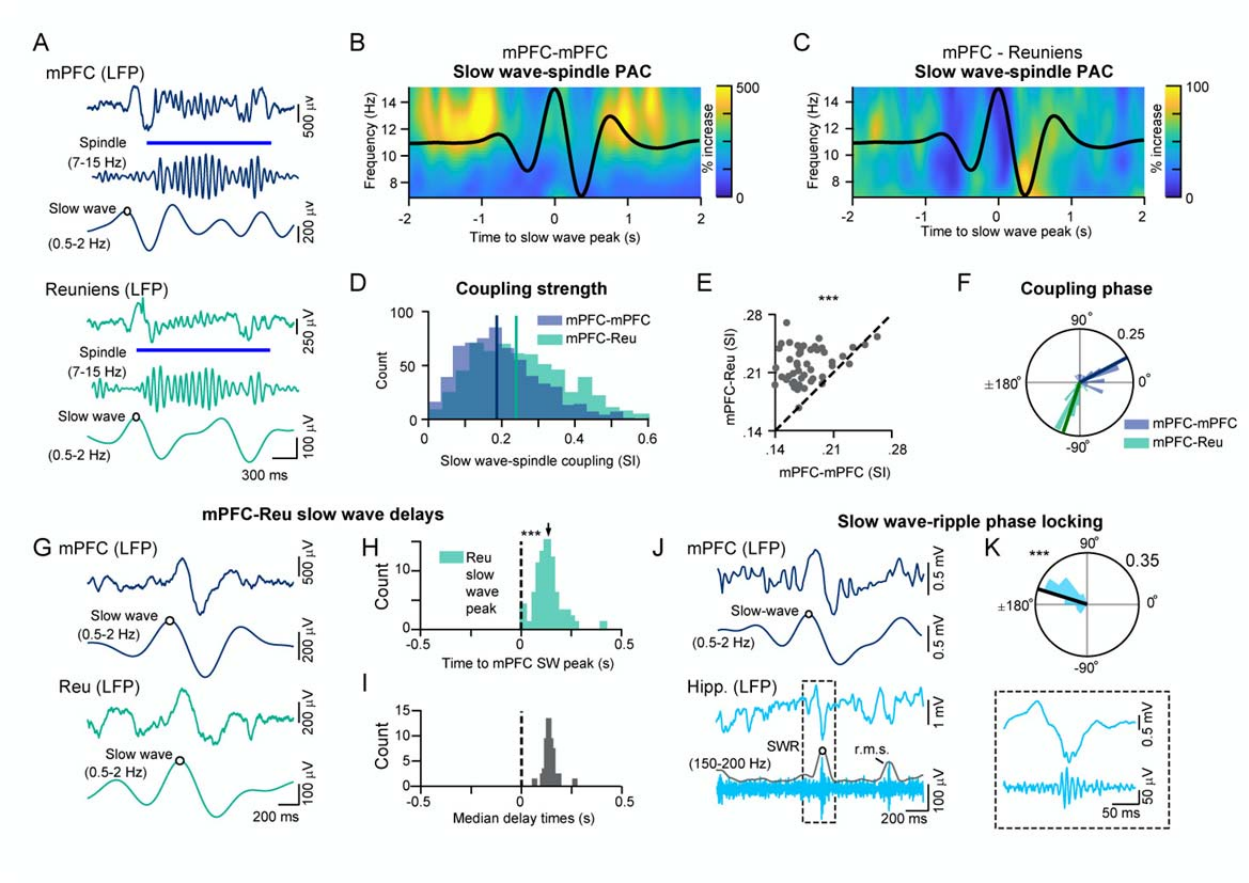

A. A single trial of a slow wave-spindle event, showing raw and filtered LFP traces of the mPFC (top) and reuniens (bottom).

B. Phase-amplitude coupling of mPFC spindles and mPFC slow waves, shown as the average time-frequency representation of mPFC amplitudes in the spindle frequency range, locked to the peak of the mPFC slow wave (percentage change from pre-event baseline, n = 626 slow waves).

1026 C. Phase-amplitude coupling of reuniens spindles and mPFC slow waves, shown as the
1027 average time-frequency representations of reuniens amplitudes, locked to the peak of
1028 the same mPFC slow waves as in B (percentage change from pre-event baseline, n = 626
1029 slow waves). Black curves in B and C show the average of the mPFC LFP, filtered in the
1030 slow wave frequency range (0.5-2Hz).

1031 D. Histogram of slow wave–spindle coupling strengths for mPFC slow waves-mPFC spindles
1032 (blue) and mPFC slow wave-reuniens spindles (green). Vertical lines indicate the median
1033 of the distributions (median ± MAD, SI strength = 0.18 ± 0.09 and 0.24 ± 0.11 for mPFC
1034 and reuniens spindles, respectively, $p = 2.126 \times 10^{-17}$, Wilcoxon signed rank test).

1035 E. Slow wave-spindle coupling strength of mPFC-mPFC pairs versus mPFC-reuniens pairs (n
1036 = 49 sessions, $p = 3.39 \times 10^{-2}$, Wilcoxon signed rank test). Each circle represents one
1037 session.

1038 F. Population data showing the relative preference of spindles to the phase of the mPFC
1039 slow wave, shown as a histogram of SI angle means for mPFC slow wave- mPFC spindle
1040 coupling and mPFC slow wave-reuniens spindle coupling (mean ± SD = 27.92 ± 37.59°, p
1041 $= 4.661 \times 10^{-9}$, n=26 and mean ± SD = -108.48 ± 21.17°, $p = 1.278 \times 10^{-20}$, n = 36, for
1042 mPFC and reuniens respectively, Rayleigh test).

1043 G. A single trial of an overlapping slow waves, showing raw and filtered LFP traces of the
1044 mPFC (top) and reuniens (bottom). Circles indicate slow wave peaks.

1045 H. Single session data, showing the distribution of delays between reuniens and mPFC slow

1046 waves (vertical dashed line). Reuniens slow waves lagged mPFC slow waves (median ±

1047 MAD = 0.126 ± 0.043 s, $p = 3.66 \times 10^{-15}$, n = 82 Wilcoxon signed rank test).

1048 I. Population data of median delay times between each reuniens-mPFC slow wave pair

1049 (n=49 sessions, median of the distribution = 0.136 s).

1050 J. Single-trial of raw and filtered mPFC and hippocampal LFPs during one overlapping slow

1051 wave-SWR event. Inset shows an expanded view of the detected SWR.

1052 K. Circular histogram of mPFC slow wave phases at the time of SWRs (mean phase ± SD =

1053 162.7 ± 29.37°, $p = 5.02 \times 10^{-6}$, Rayleigh test).

1054 *p < 0.05, **p <0.01, ***p<0.001.

1055 See also Figure 3 – figure supplement 1 for spindle-SWR coupling.

1056

1057

1058

1059 **Figure 4 Hippocampal theta oscillations and SWRs modulate reuniens activity**

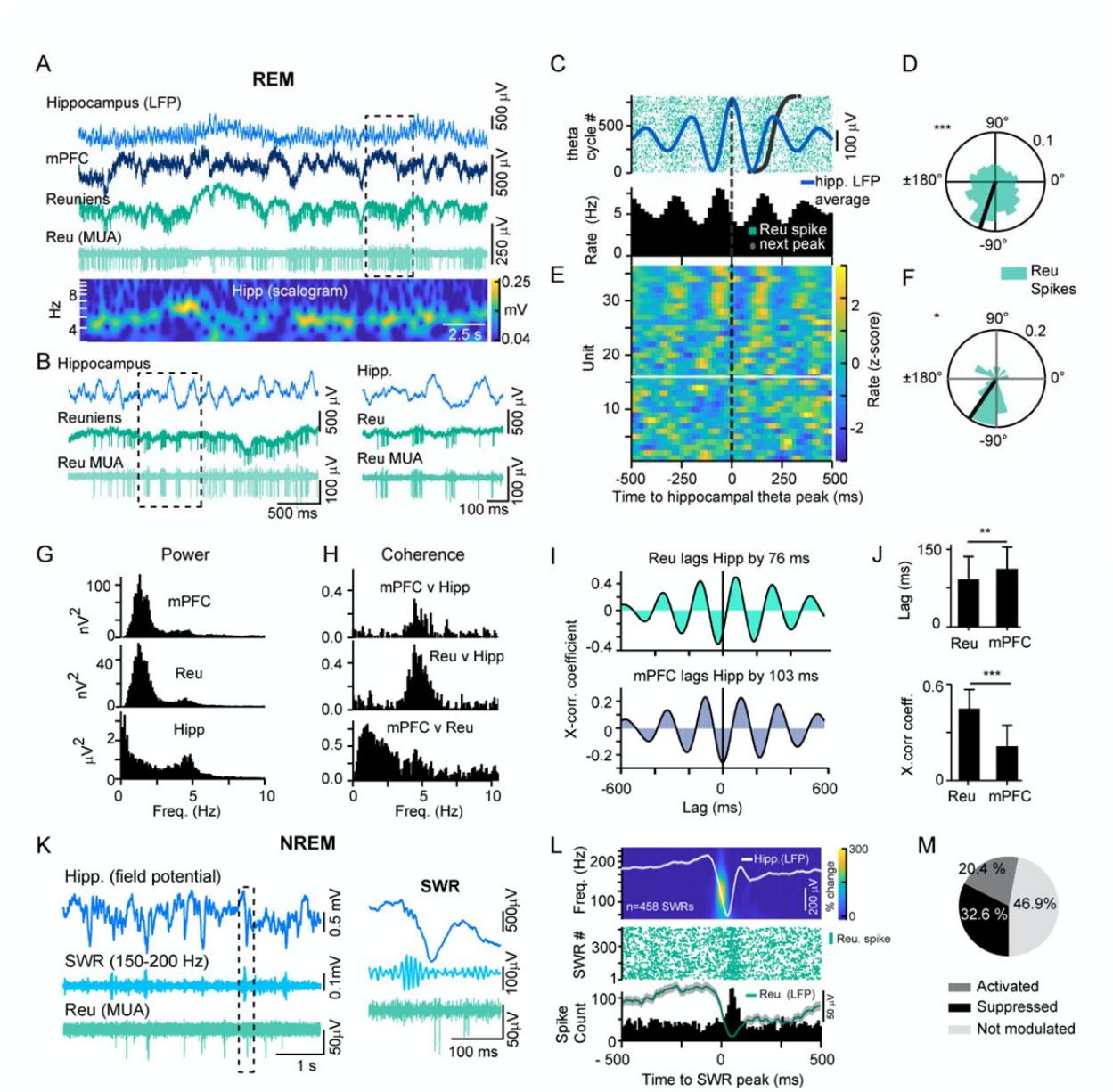

1060

1061 A. Representative example of LFP recordings of the hippocampus, mPFC and reuniens

1062 during REM sleep (top three traces) and the bandpassed (300-8000 Hz) trace of the

1063 reuniens signal showing multiunit activity. Wavelet spectrogram of the hippocampal

1064 trace, showing prominent theta-band activity during REM. The frequency axis is
1065 logarithmic.

1066 B. Expanded view of the recording epoch in the dotted-line box in panel A (left), further
1067 expanded in time (right), showing occasional locking of reuniens multi-unit activity to
1068 hippocampal theta cycles.

1069 C. Peri-event histogram of a reuniens single-unit, referenced to the peak of hippocampal
1070 theta cycles (top). The raster is ordered according to the peak-to-peak latency, with
1071 short periods at the bottom and long periods at the top. Dark black dots indicate the
1072 timing of the next peak in the trial. The light blue trace is the average waveform of the
1073 hippocampal LFP.

1074 D. Circular histogram of theta phase at the time of reuniens spikes, showing significant
1075 phase-locking of reuniens single-unit activity to hippocampal theta cycles (n = 5207
1076 spikes, $p<10^{-20}$, Rayleigh test).

1077 E. Population data, showing peri-event histograms referenced to the peak of hippocampal
1078 theta cycles as in B (n=36 single units). Units above the white line were significantly
1079 modulated by hippocampal theta cycles.

1080 F. Population data, showing the circular distribution of reuniens firing relative to theta
1081 cycles for all modulated single units (n = 21/36 single-units, mean ± SD = -124.5 ± 59.8 °,
1082 p = 0.011, Rayleigh test).

1083 G. Single session data, showing power spectra of mPFC, reuniens and hippocampal signals
1084 during REM with prominent peaks in the theta range.

1085 H. Single session data, showing signal coherence between mPFC-hippocampus, reuniens-
1086 hippocampus and mPFC-reuniens recording pairs during REM.

1087 I. Single session data, showing cross-correlations and relative time lags of reuniens-
1088 hippocampus and mPFC-hippocampus recording pairs during REM.

1089 J. mPFC signals lagged hippocampal theta signal by longer delay than reuniens signals
1090 lagged hippocampus (top, mean lag ± SD = 87.8 ± 55.5 ms and 109.1 ± 41.52 for
1091 reuniens and mPFC, respectively, n=20 sessions, p=0.002, t-test). Peak cross-correlation
1092 coefficients were significantly higher for reuniens-Hippocampus recording pairs than for
1093 reuniens-mPFC (bottom, mean peak value ± SD = 0.44 ± 0.13 and 0.22 ± 0.07 for
1094 reuniens and mPFC respectively=20 sessions, t-test, $p<10^{-20}$).

1095 K. Representative LFP recordings of the hippocampus and of reuniens multiunit activity
1096 during NREM sleep. Light blue traces show the bandpass filtered hippocampal recording
1097 in the ripple band (150-200 Hz). Light green shows multiunit activity in reuniens during
1098 SWR. Expanded view of a single SWR from the recording epoch in the dotted-line box
1099 and multiunit activity in reuniens.

1100 L. Peri-event analysis of reuniens spiking activity around SWRs in one recording session.
1101 The time frequency representation shows the mean wavelet transform of 458 detected
1102 SWRs, estimated by Morlet wavelets (top). Overlayed traces show the grand average

1103 LFP in the hippocampus (white) and reuniens (green), referenced to the onset of the

1104 SWR. Raster of reuniens spikes (every 10th sweep) and associated peri-event spike

1105 histogram, referenced to the onset of the SWR (bottom).

1106 M. Proportion of reuniens single-units modulated by SWRs (10/49 activated, 16/49

1107 suppressed).

1108 *$p < 0.05$, **$p < 0.01$, ***$p < 0.001$.

1109

1110

Figure 5 Multiregional temporal interactions during slow wave sleep events in a hippocampal-thalamocortical model

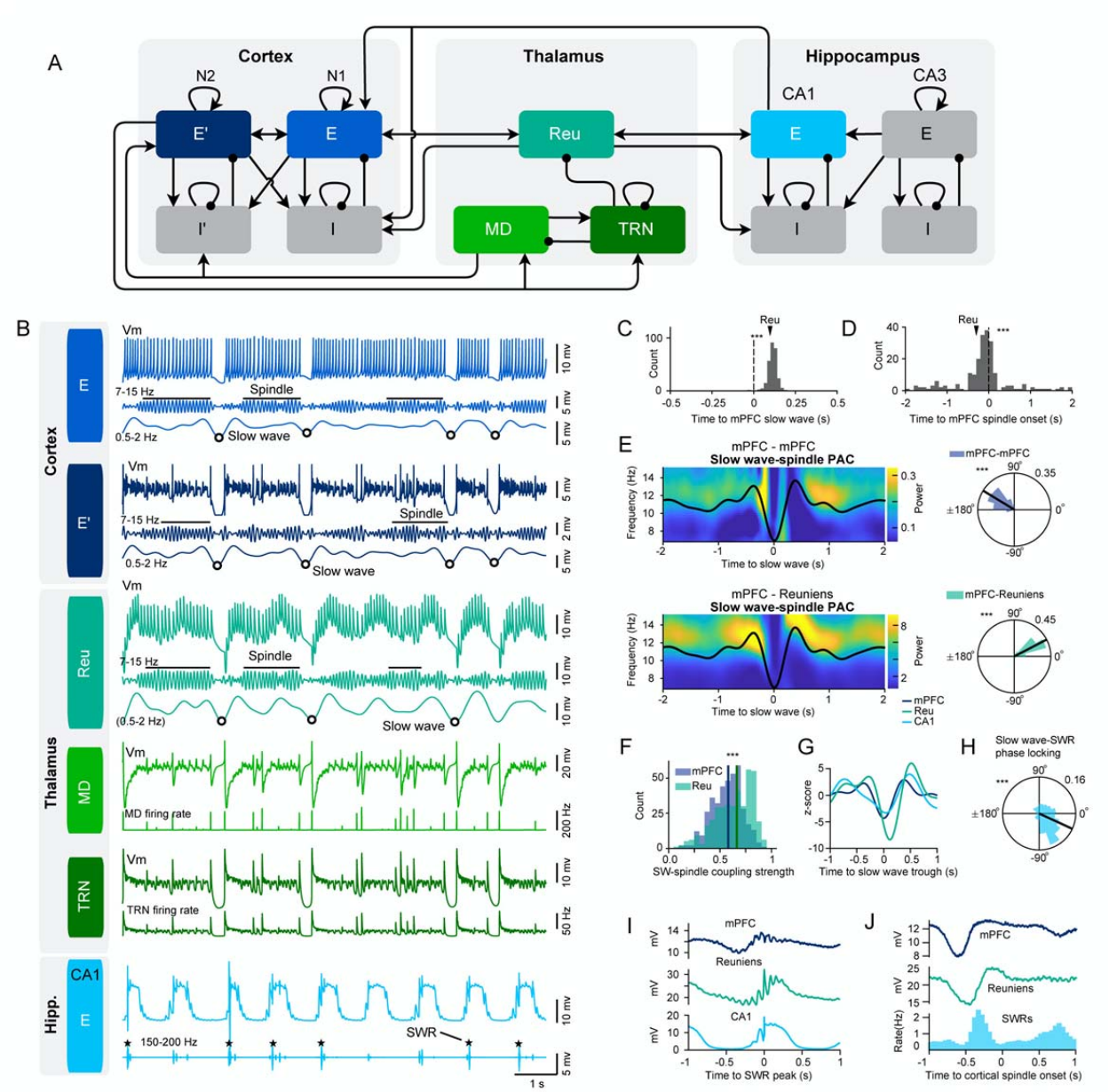

A. The model is composed of two cortical networks (N 1 & 2, representing mPFC layers 5 and 6 respectively), two hippocampal (CA1-CA3) networks and three thalamic nuclei. The three thalamic networks represent the nucleus reuniens (Reu), mediodorsal

thalamic nucleus (MD) and thalamic reticular nucleus (TRN). The cortical and hippocampal networks are composed of one group of identical excitatory (E) and one group of identical inhibitory (I) neurons. Excitatory synaptic connections are shown by arrows and inhibitory connections are indicated as lines ending in a dot.

B. From top to bottom: broadband and filtered (7-15 Hz, 0.5-2 Hz) traces of the membrane potential of excitatory neurons of cortical network 1 (light blue) and 2 (dark blue) with detected spindles (black horizontal lines) and slow waves (circles); broadband and filtered (7-15 Hz, 0.5-2 Hz) traces of the membrane potential of reuniens neurons (blue-green) with detected spindles and slow waves; broadband trace of the membrane potential and firing rate of MD (light green) and reticular neurons (dark green); broadband and filtered (150-200 Hz) traces of the membrane potential of excitatory neurons of the CA1 network (light blue) with detected SWRs (stars).

C. Distribution of thalamic slow wave troughs (down states) locked to the cortical slow wave trough (vertical dashed line at zero) occurring within ±0.5 s plotted in 20 ms bins in the model. The arrow indicates the median of the distribution (n = 277, median ± MAD = 0.113 ± 0.019 s). Thalamic slow waves occur significantly later than cortical slow waves ($p < 10^{-20}$, Wilcoxon signed rank test).

D. Distribution of thalamic spindle onsets locked to the cortical spindle onset (vertical dashed line at zero) occurring within ±2 s plotted in 100 ms bins for one session. The arrow indicates the median of the distribution (n = 211, median ± MAD = -0.102 ± 0.387

s). Thalamic spindles occur significantly earlier than cortical spindles ($p = 1.30 \times 10^{-7}$, Wilcoxon signed rank test).

E. Phase-amplitude coupling of slow waves and spindles, calculated from the average time-frequency representation of amplitudes in the spindle frequency range, locked to the trough of the mPFC slow wave. Left, average of cortical slow wave trough-locked time-frequency representations (n =391) of the membrane potential of mPFC excitatory neurons (top) and reuniens neurons (bottom). Black curves represent grand average filtered membrane potential of cortical excitatory neurons in the slow wave frequency range (0.5-2 Hz) aligned to the cortical slow wave trough (time 0). Right, circular histogram of synchronization index (SI) angles of cortical (top) and reuniens (bottom) spindles relative to the cortical slow waves. SI angles were nonuniformly distributed (mean ± SD = 148.7 ± 23.9°, $p < 10^{-20}$ and mean ± SD = 27.4 ± 20.4°, $p < 10^{-20}$, for mPFC and reuniens respectively, Rayleigh test, n=391 slow waves).

F. Histogram of the slow wave–spindle coupling strengths (the absolute value of the synchronization index) for mPFC (blue) and reuniens (green) spindles. Vertical lines show the median of the distribution ($p = 8.45\times 10^{-9}$, Wilcoxon signed rank test, median ± MAD SI strength = 0.58 ± 0.11 and 0.66 ± 0.15 for mPFC and reuniens, respectively).

G. Average filtered membrane potential of cortical, reuniens and CA1 excitatory neurons, in the slow wave frequency range (0.5-2 Hz), aligned to the cortical slow wave trough (time 0).

1157 H. Distribution of slow wave phases at the time of the SWRs. Zero phase shows the peak

1158 (up state) of slow waves (n = 714, mean ± SD = -24.97 ± 62.01°, $p < 10^{-20}$, Rayleigh test).

1159 I. Average membrane potential of the mPFC, reuniens and CA1 excitatory neurons aligned

1160 to the SWR peaks.

1161 J. Average membrane potential of the mPFC (top) and reuniens (middle) neurons and

1162 histogram of SWR incidence (bottom), aligned to the onset of cortical spindles.

1163 *p < 0.05, **p <0.01, ***p<0.001.

1164

1165

Figure 6 Bidirectional projections between the reuniens and CA1 control multiregional interactions

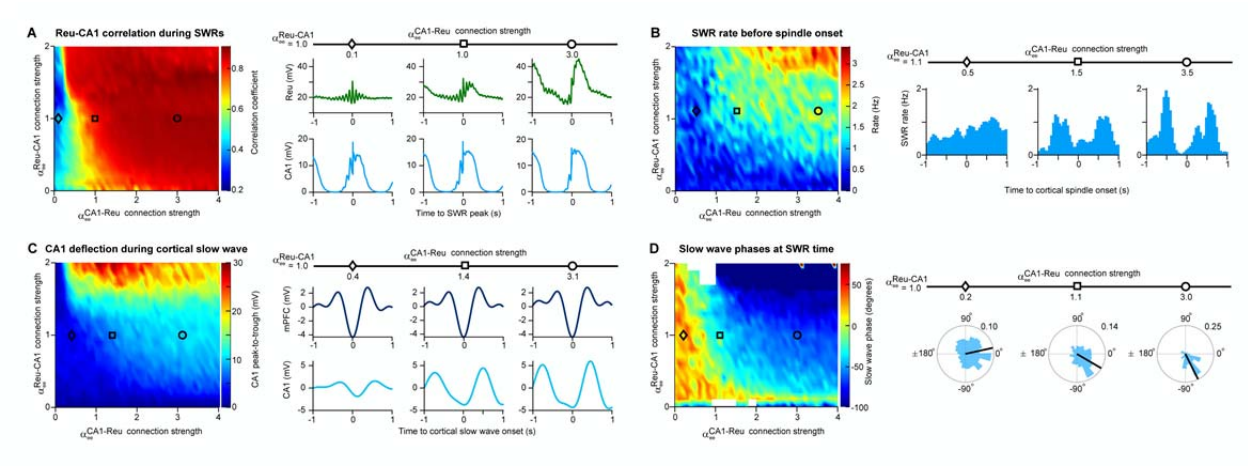

A. Left, correlation between reuniens and CA1 membrane potentials during SWRs (maximum value of the covariance between reuniens and CA1 membrane potentials ± 0.5 s around the SWR peak) versus the CA1-reuniens and reuniens-CA1 connection strengths ($\alpha_{ee}^{CA1-Reu}$ and $\alpha_{ee}^{Reu-CA1}$ show the factor multiplied to $J_{ee}^{CA1-Reu}$ and $J_{ee}^{Reu-CA1}$ representing the strength of the input from CA1 to reuniens and from reuniens to excitatory neurons of CA1 respectively. $\alpha_{ee}^{CA1-Reu}$ = $\alpha_{ee}^{Reu-CA1}$ = 1 corresponds to the network shown in **Figure 5**). Right, average traces of the reuniens and CA1 membrane potentials aligned to the SWR peaks for 3 different values of CA1-reuniens connection strengths.

B. Left, SWR rate preceding the cortical spindle onset (peak-to-trough of the histogram of SWR incidence in a window of -1 s before the spindle onset) versus the CA1-reuniens and reuniens-CA1 connection strengths. Right, histogram of SWR incidence time-locked

to the onset of cortical spindles for 3 different values of CA1-reuniens projection strengths.

C. Left, peak-to-trough of the CA1 deflections around cortical slow wave trough (± 1 s) versus the CA1-reuniens and reuniens-CA1 connection strengths. Right, average filtered membrane potential of cortical, and CA1 excitatory neurons, in the slow wave frequency range (0.5-2 Hz) aligned to the cortical slow wave trough (time 0) for 3 different values of CA1-reuniens connection strengths.

D. Left, mean slow wave phase at the time of SWRs versus the CA1-reuniens and reuniens-CA1 connection strengths. Mean phases are shown only for bins with nonuniformly distributed of phases ($p < 0.05$, Rayleigh test) and omitted for uniformly distributed phase (white boxes). Right, histogram of slow wave phases at the time of SWRs for 3 different values of CA1-reuniens connection strengths, showing decreasing mean phase with increasing CA1-reuniens connections strength ($p = 4.28 \times 10^{-8}$, $p = 7.53 \times 10^{-15}$ and $p = 2.53 \times 10^{-39}$ for $\alpha_{ee}^{CA1-Reu} = 0.2$, 1.1 and 3.0, respectively).

1196 **Figure 2 – figure supplement 1 Single-unit detection method from tetrode recordings**

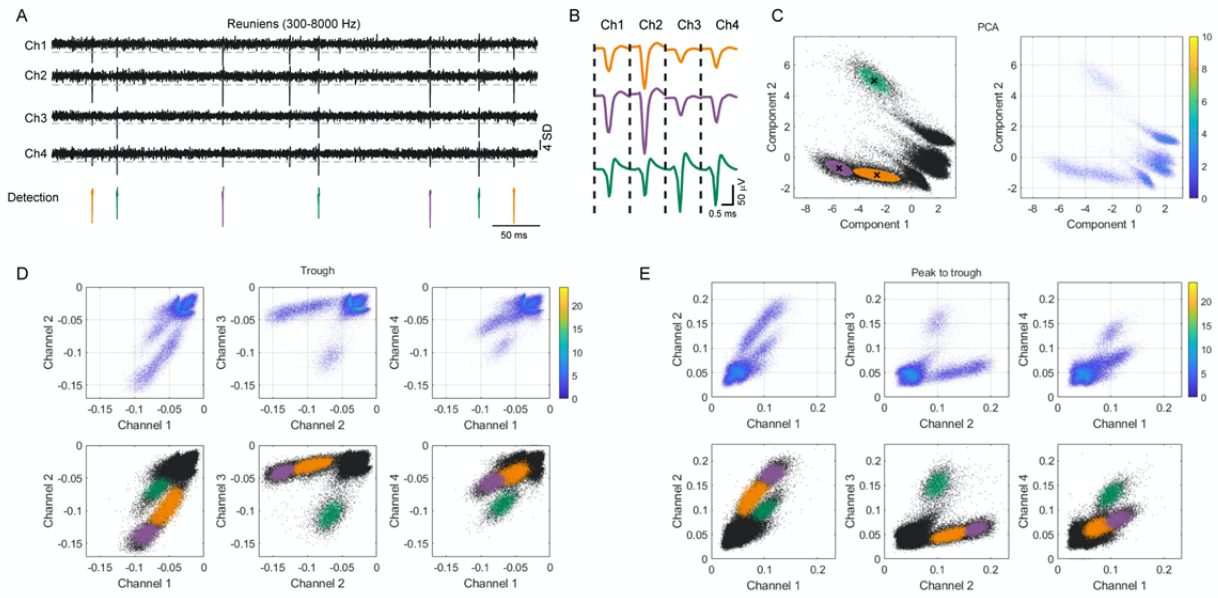

1197

1198 A. Illustrative example of reuniens LFPs with spiking activity, recorded by 4 closely-spaced
1199 electrodes in tetrode configuration. Recordings show the bandpass (300-8000 Hz)
1200 filtered traces of from 4 channels and detected spikes.

1201 B. Average waveforms of detected spikes, sorted according to clustering of waveform
1202 features extracted from the each of the 4 channels.

1203 C. Example of feature clustering for the same recording session as above, showing the
1204 principal components 1 versus principal component 2. Clusters were determined by a
1205 Gaussian mixture model and further refined by removing spikes with large Mahalanobis
1206 distance. Separated clusters indicate three classes of spike waveforms, presumed to
1207 have been generated by three distinct neurons (purple, green and pink).

1208 D. Cluster separation for trough values for the same session as above.

E. Cluster separation for the peak-to-trough values for the same session as above.

Figure 3 – figure supplement 1 Spindle-SWR phase locking

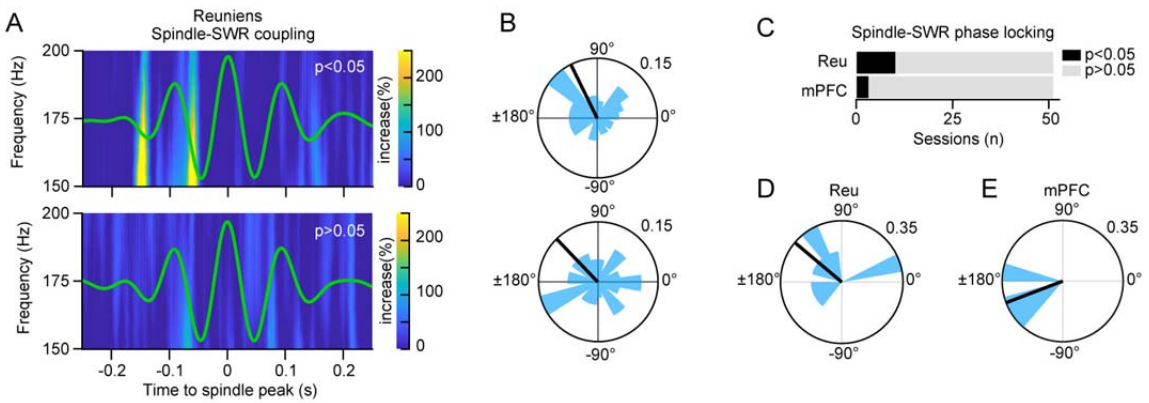

A. Assessment of SWR phase-locking to reuniens spindle cycles for sessions with significant (top) and not significant (bottom) phase-locking. The TFR shows the average hippocampal LFP in the ripple band, as percent change from pre-event baseline, referenced to the peak of the reuniens spindle (time 0) . Green curve shows grand average of the reuniens LFP, filtered in the spindle frequency range (7-15 Hz).

B. Circular histogram of SI angles of SWR amplitude relative to reuniens spindle phase for the same two sessions as in A, showing significant (p = 0.009, Rayleigh test) and not significant phase-locking (p = 0.893, Rayleigh test)

C. Proportion of recording sessions with significant SWR-reuniens spindle coupling phase.

D. Population data of sessions with significant SWR-reuniens spindle coupling phase, showing the phase histogram of SWR amplitude with respect to spindle cycles and the mean phase preference (black line, n = 10).

1225 E. The same as D for SWR-mPFC spindle coupling (n = 3).

1226

1227 **Table 1 Spindle-SWR coupling, p-values per session.**

Recording Session	Recording Duration (s)	Sleep Duration (s)	**mPFC-hipp** p-val.	**Reu-hipp** p-val.
Amande_Day6S2	5888	1460	0.273	0.786
Amande_Day7S1	8210	720	0.726	0.718
Amande_Day7S2	3573	2180	0.74	0.204
Amande_Day8S1	8343	720	0.202	**0.022**
Amande_Day8S2	5734	1900	0.505	0.927
Amande_Day8S3	5693	1420	0.65	0.725
Amande_Day9S1	4543	660	**0.039**	0.875
Amande_Day9S2	4413	1560	0.757	0.866
Amande_Day9S3	4943	3640	0.964	0.066
Amande_Day10S1	3163	240	0.318	0.772
Amande_Day10S2	6488	4560	0.767	0.152
Amande_Day11S1	3033	440	0.068	0.429
Amande_Day11S2	9016	4710	0.594	**0.019**
Cocotte_Day4S1	6763	1900	0.155	0.034
Cocotte_Day4S2	4033	1000	0.081	0.505
Cocotte_Day5S1	6423	1720	0.975	0.427

Cocotte_Day6S1	6043	580	0.72	**0.013**
Cocotte_Day6S2	6033	1780	0.429	0.571
Cocotte_Day7S1	5965	2160	0.494	0.681
Cocotte_Day7S2	4190	1580	0.617	0.78
Cocotte_Day7S3	5495	2700	0.91	0.139
Cocotte_Day8S1	8389	5480	0.449	**6.36E-04**
Cocotte_Day8S2	6578	4700	0.476	**0.019**
Cocotte_Day8S3	2588	720	0.798	0.619
Cocotte_Day9S1	10073	6520	0.937	0.174
Cocotte_Day9S2	5289	2740	0.581	**0.046**
Cocotte_Day10S1	4583	480	0.142	0.957
Cocotte_Day10S2	5953	4100	0.358	0.624
Cocotte_Day10S3	6018	2280	0.667	0.386
Cocotte_Day11S1	14023	9680	0.055	0.104
Cocotte_Day12S1	9863	6840	0.646	0.928
Garfield_Day4S2	3428	940	0.187	0.234
Garfield_Day4S3	4753	1720	**0.003**	0.013
Garfield_Day5S1	8439	1920	0.737	0.345
Garfield_Day5S2	6464	2680	0.123	0.557
Garfield_Day6S1	8073	2080	0.396	0.781

Garfield_Day6S2	7073	4400	0.065	0.895
Garfield_Day7S1	8623	2700	0.619	0.494
Garfield_Day7S2	6664	4360	0.277	**0.002**
Garfield_Day8S1	4884	340	0.775	0.929
Garfield_Day8S2	5468	2520	0.556	0.237
Garfield_Day8S3	4438	3020	0.497	0.319
Garfield_Day9S1	4438	2980	0.3	0.248
Garfield_Day9S2	4568	1780	0.321	0.43
Garfield_Day9S3	6329	3680	**0.029**	**0.013**
Garfield_Day10S1	7068	840	0.719	0.409
Garfield_Day10S2	1089	120	0.459	0.135
Garfield_Day11S1	6684	1980	0.857	0.258
Garfield_Day12S1	5893	1520	0.538	0.971
Garfield_Day12S2	7503	3360	0.633	0.701
Garfield_Day13S1	3063	300	0.296	0.466

Bold indicates significant values.

Article and author information

Author Details

Diellor Basha

Département de psychiatrie et de neurosciences, Université Laval, Québec, QC,Canada

CERVO Centre de recherche, Université Laval, Québec, QC, Canada

Contribution: Conceptualization, Methodology, Investigation, Software, Visualization, Formal Analysis, Data Curation, Writing - Original Draft

Competing interests: No competing interests declared.

Amirmohammad Azarmehri

Department of Electrical Engineering, Ferdowsi University of Mashhad, Mashhad, Iran

Contribution: Methodology, Software, Visualization, Formal Analysis, Writing-Original Draft

Competing interests: No competing interests declared.

Eliane Proulx

Département de psychiatrie et de neurosciences, Université Laval, Québec, QC,Canada

Current address: CNS Diseases Research, Boehringer Ingelheim Pharma GmbH & Co. KG, Biberach an der Riß, Baden-Württemberg, Germany

Contribution: Methodology, Investigation, Visualization, Formal Analysis, Data Curation, Writing – Original Draft

Competing interests: No competing interests declared.

Sylvain Chauvette

CERVO Centre de recherche, Université Laval, Québec, QC, Canada

Contribution: Methodology, Investigation, Validation, Resources, Writing - Review & Editing

Competing interests: No competing interests declared.

Maryam Ghorbani

Department of Electrical Engineering, Ferdowsi University of Mashhad, Mashhad, Iran

Contribution: Conceptualization, Methodology, Investigation, Validation, Writing - Review & Editing, Supervision, Project administration

Competing interests: No competing interests declared.

Igor Timofeev

Département de psychiatrie et de neurosciences, Université Laval, Québec, QC,Canada

CERVO Centre de recherche, Université Laval, Québec, QC, Canada

Contribution: Conceptualization, Methodology, Investigation, Validation, Writing - Review & Editing, Supervision, Project administration, Funding Acquisition.

Competing interests: No competing interests declared.

For correspondence: igor.timofeev@fmed.ulaval.ca

Centre de recherche CERVO, 2601 de la Canardiere Quebec, QC, Canada

Funding

National Sciences and Engineering Research Council of Canada (grant RGPIN-2018-06291)

Igor Timofeev

Canadian Institutes of Health Research (grants PTJ - 183862)

Igor Timofeev

Acknowledgements

We thank Serge Ftomov for technical assistance.

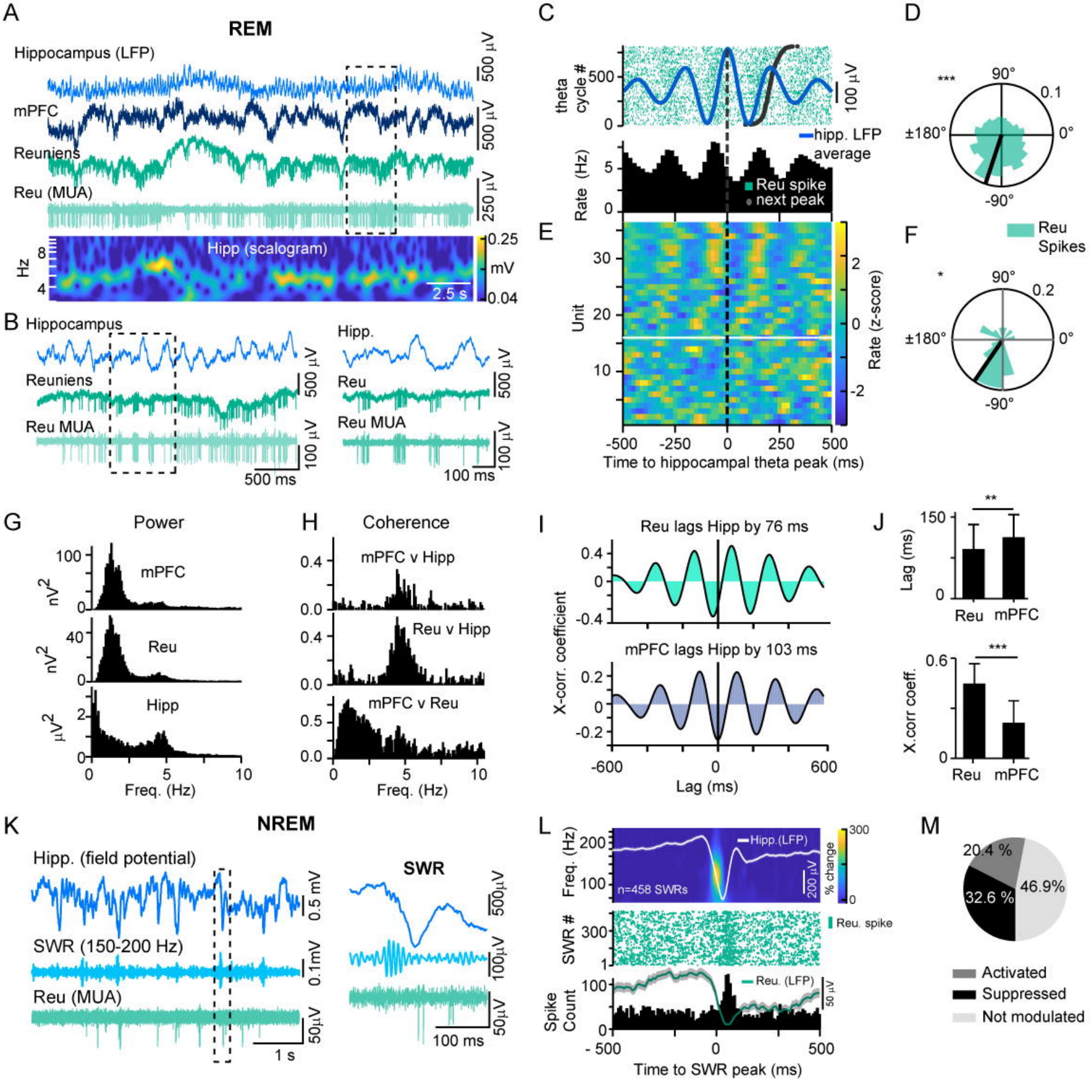
A
REM
Hippocampus (LFP)
mPFC
Reuniens
Reu (MUA)
Hipp (scalogram)
Hz
8
4
0.25
mV
0.04
2.5 s
500 µV
500 µV
250 µV
B
Hippocampus
Reuniens
Reu MUA
500 µV
100 µV
500 ms
Hipp.
Reu
Reu MUA
500 µV
100 µV
100 ms
C
theta cycle #
500
0
100 µV
hipp. LFP average
Rate (Hz)
5
0
Reu spike
next peak
E
Unit
30
20
10
2
0
-2
Rate (z-score)
-500
-250
0
250
500
Time to hippocampal theta peak (ms)
D
***
90°
0.1
±180°
0°
-90°
F
Reu Spikes
*
90°
0.2
±180°
0°
-90°
G
Power
mPFC
Reu
Hipp
nV²
nV²
µV²
100
40
2
0
0
0
5
10
Freq. (Hz)
H
Coherence
mPFC v Hipp
Reu v Hipp
mPFC v Reu
0.4
0.0
0.4
0.0
0.5
0.0
0
5
10
Freq. (Hz)
I
Reu lags Hipp by 76 ms
mPFC lags Hipp by 103 ms
X-corr. coefficient
0.4
0
-0.4
0.2
0
-0.2
-600
0
600
Lag (ms)
J
**
150
0
Lag (ms)
Reu
mPFC
***
0.6
0
X.corr coeff.
Reu
mPFC
K
NREM
Hipp. (field potential)
SWR (150-200 Hz)
Reu (MUA)
0.5 mV
0.1mV
50µV
1 s
SWR
500µV
100µV
50µV
100 ms
L
Freq. (Hz)
200
100
Hipp.(LFP)
n=458 SWRs
200 µV
% change
300
0
SWR #
300
1
Reu. spike
Spike Count
100
0
Reu. (LFP)
50 µV
- 500
0
500
Time to SWR peak (ms)
M
20.4 %
46.9%
32.6 %
Activated
Suppressed
Not modulated

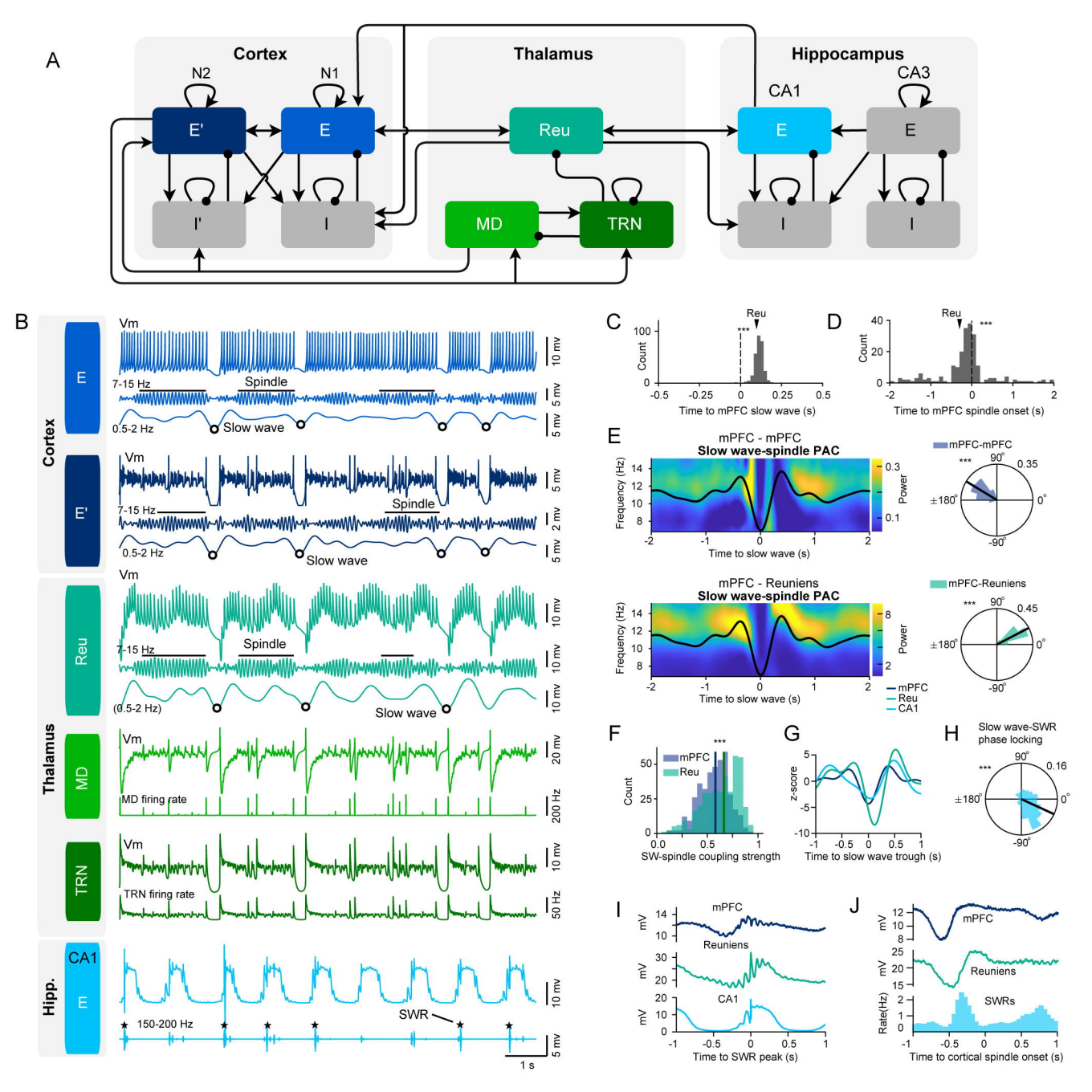
A
Cortex
Thalamus
Hippocampus
N2
N1
CA1
CA3
E'
E
Reu
E
E
I'
I
MD
TRN
I
I
B
Cortex
Thalamus
Hipp.
E
E'
Reu
MD
TRN
CA1
Vm
7-15 Hz
Spindle
0.5-2 Hz
Slow wave
(0.5-2 Hz)
MD firing rate
TRN firing rate
150-200 Hz
SWR
10 mv
5 mv
2 mv
20 mv
200 Hz
50 Hz
1 s
C
Reu
Count
Time to mPFC slow wave (s)
D
Reu
Count
Time to mPFC spindle onset (s)
E
mPFC - mPFC
Slow wave-spindle PAC
Frequency (Hz)
Power
Time to slow wave (s)
mPFC-mPFC
mPFC - Reuniens
Slow wave-spindle PAC
mPFC-Reuniens
mPFC
Reu
CA1
F
mPFC
Reu
Count
SW-spindle coupling strength
G
z-score
Time to slow wave trough (s)
H
Slow wave-SWR phase locking
I
mPFC
Reuniens
CA1
mV
Time to SWR peak (s)
J
mPFC
Reuniens
SWRs
mV
Rate(Hz)
Time to cortical spindle onset (s)

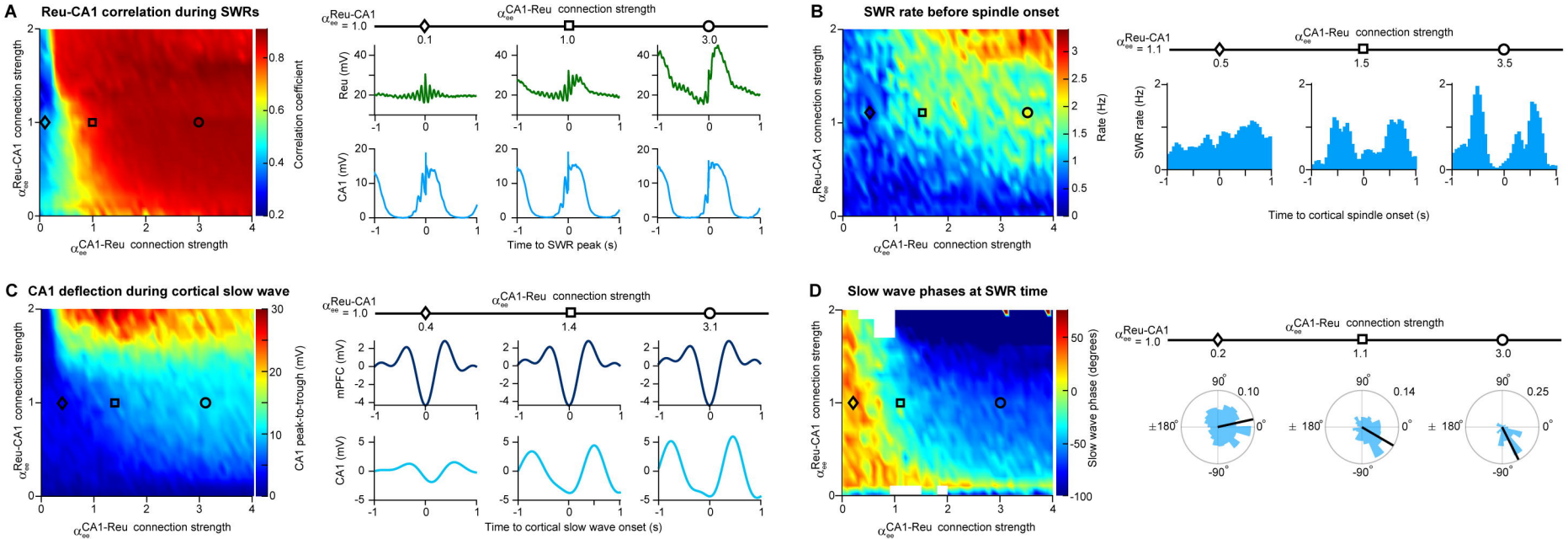
A
Reu-CA1 correlation during SWRs
Correlation coefficient
Reu (mV)
CA1 (mV)
Time to SWR peak (s)
B
SWR rate before spindle onset
Rate (Hz)
SWR rate (Hz)
Time to cortical spindle onset (s)
C
CA1 deflection during cortical slow wave
CA1 peak-to-trough (mV)
mPFC (mV)
CA1 (mV)
Time to cortical slow wave onset (s)
D
Slow wave phases at SWR time
Slow wave phase (degrees)
CA1-Reu connection strength
Reu-CA1 connection strength

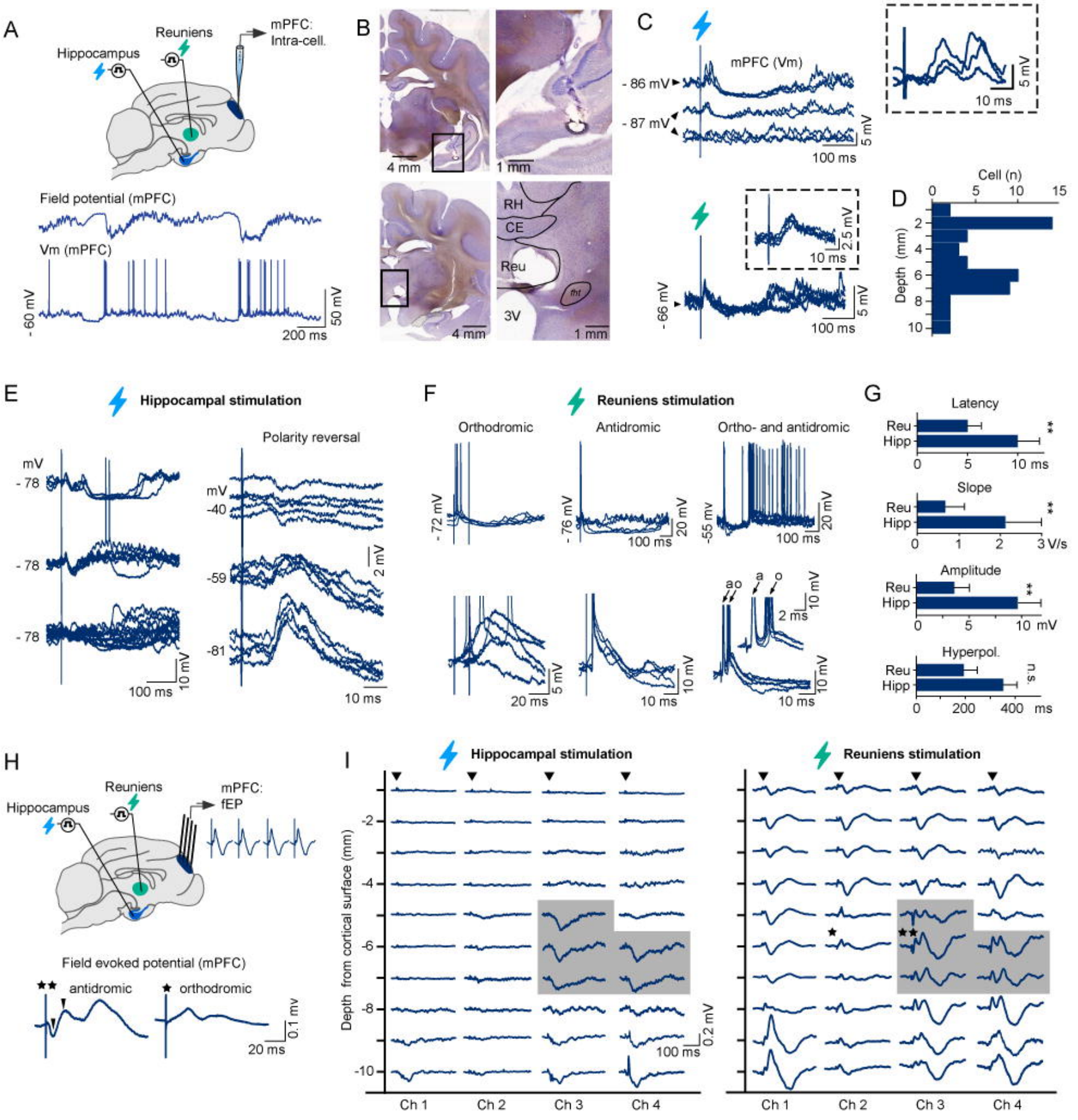
A
Reuniens
mPFC:
Intra-cell.
Hippocampus
Field potential (mPFC)
Vm (mPFC)
- 60 mV
50 mV
200 ms
B
4 mm
1 mm
RH
CE
Reu
3V
fmt
C
mPFC (Vm)
- 86 mV
- 87 mV
5 mV
100 ms
10 ms
- 66 mV
2.5 mV
D
Cell (n)
Depth (mm)
E
Hippocampal stimulation
Polarity reversal
mV
- 78
-40
-59
-81
2 mV
10 mV
100 ms
10 ms
F
Reuniens stimulation
Orthodromic
Antidromic
Ortho- and antidromic
- 72 mV
- 76 mV
-55 mv
20 mV
ao
a
o
2 ms
5 mV
20 ms
G
Latency
Reu
Hipp
Slope
V/s
Amplitude
mV
Hyperpol.
n.s.
ms
H
Reuniens
mPFC:
fEP
Hippocampus
Field evoked potential (mPFC)
antidromic
orthodromic
0.1 mv
20 ms
I
Hippocampal stimulation
Reuniens stimulation
Depth from cortical surface (mm)
0.2 mV
100 ms
Ch 1
Ch 2
Ch 3
Ch 4

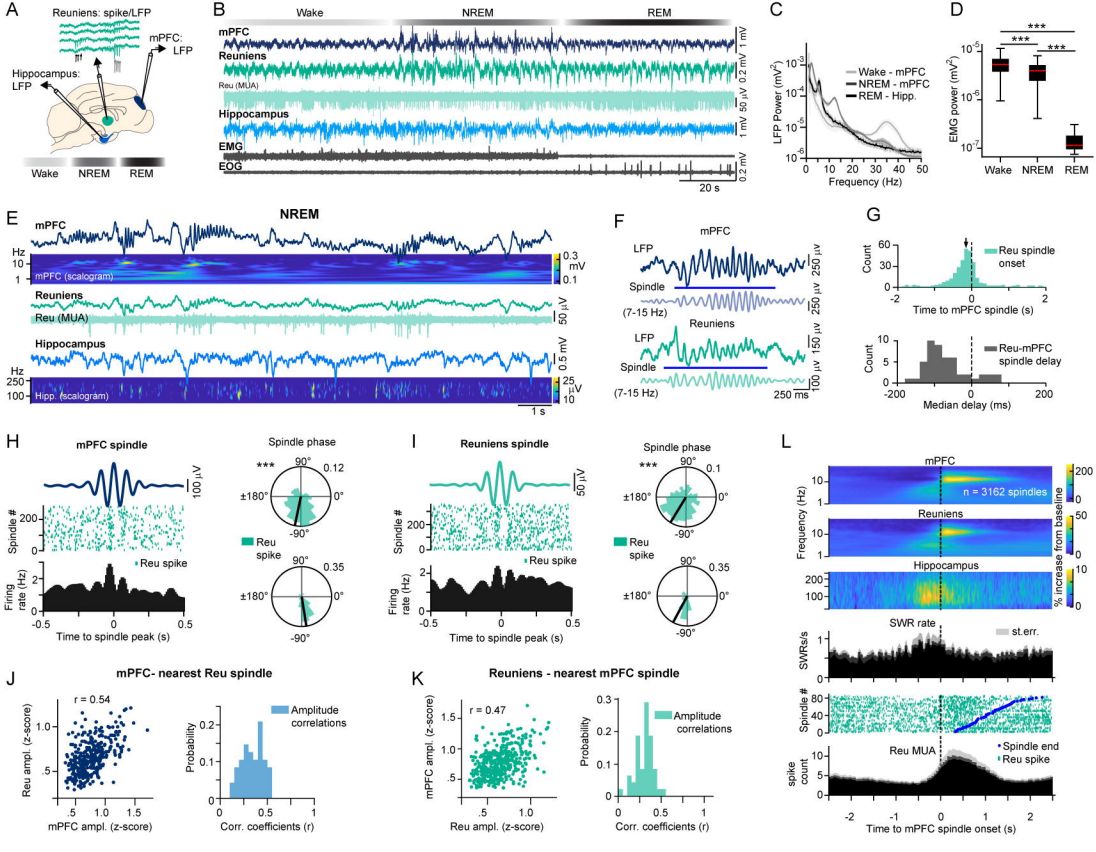
A
Reuniens: spike/LFP
mPFC: LFP
Hippocampus: LFP
Wake
NREM
REM
B
Wake
NREM
REM
mPFC
Reuniens
Reu (MUA)
Hippocampus
EMG
EOG
20 s
C
Wake - mPFC
NREM - mPFC
REM - Hipp.
LFP Power (mV²)
Frequency (Hz)
D
EMG power (mV²)
Wake
NREM
REM
E
NREM
mPFC
mPFC (scalogram)
Reuniens
Reu (MUA)
Hippocampus
Hipp. (scalogram)
1 s
F
mPFC
LFP
Spindle
(7-15 Hz)
Reuniens
250 ms
G
Reu spindle onset
Time to mPFC spindle (s)
Reu-mPFC spindle delay
Median delay (ms)
H
mPFC spindle
Spindle phase
Spindle #
Reu spike
Firing rate (Hz)
Time to spindle peak (s)
Reu spike
I
Reuniens spindle
Spindle phase
Spindle #
Reu spike
Firing rate (Hz)
Time to spindle peak (s)
Reu spike
L
mPFC
n = 3162 spindles
Reuniens
Hippocampus
Frequency (Hz)
% increase from baseline
SWR rate
st.err.
SWRs/s
Spindle #
Reu MUA
Spindle end
Reu spike
spike count
Time to mPFC spindle onset (s)
J
mPFC- nearest Reu spindle
r = 0.54
Reu ampl. (z-score)
mPFC ampl. (z-score)
Amplitude correlations
Probability
Corr. coefficients (r)
K
Reuniens - nearest mPFC spindle
r = 0.47
mPFC ampl. (z-score)
Reu ampl. (z-score)
Amplitude correlations
Probability
Corr. coefficients (r)

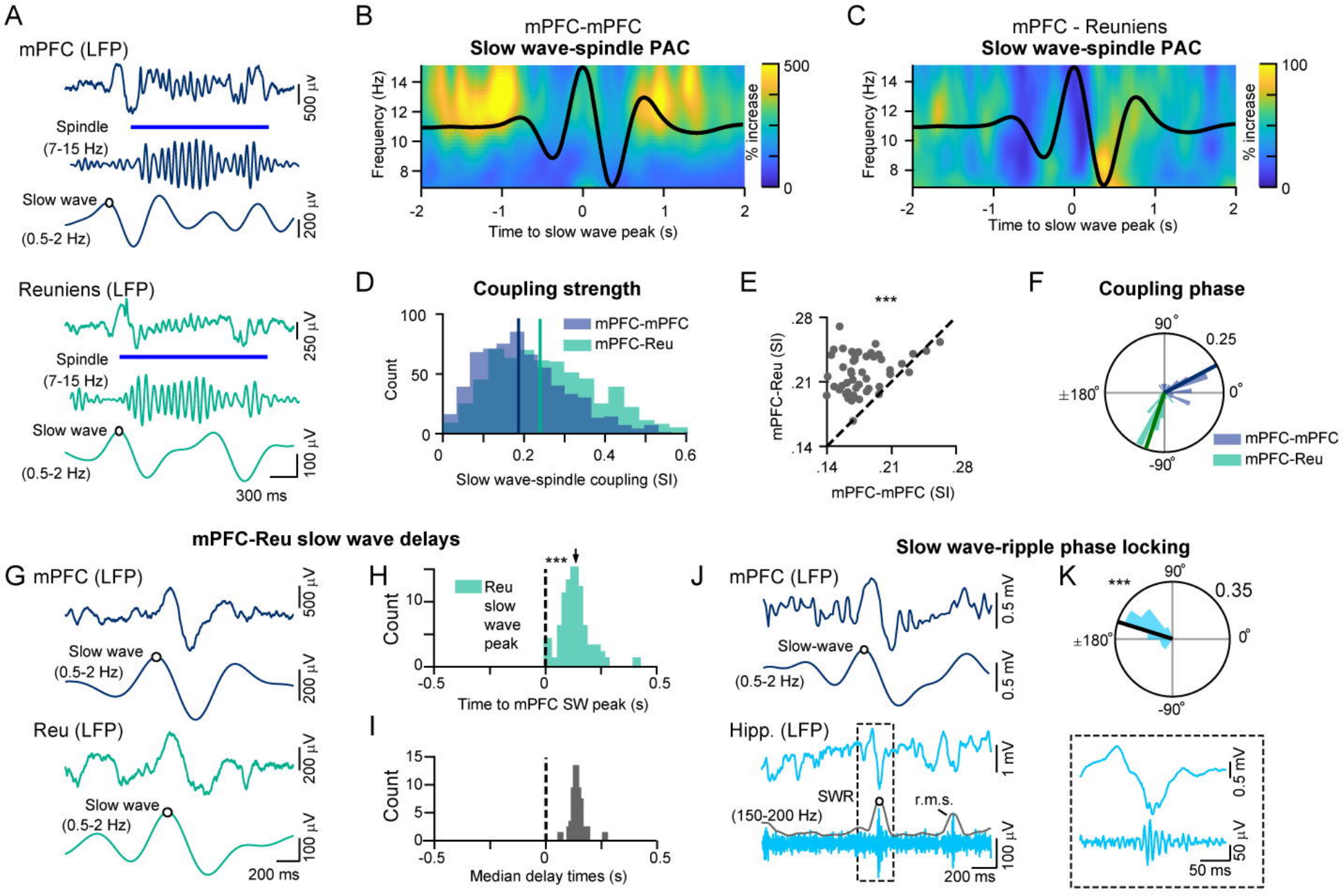
A
mPFC (LFP)
500 µV
Spindle
(7-15 Hz)
Slow wave
(0.5-2 Hz)
200 µV
Reuniens (LFP)
250 µV
Spindle
(7-15 Hz)
Slow wave
(0.5-2 Hz)
100 µV
300 ms
B
mPFC-mPFC
Slow wave-spindle PAC
Frequency (Hz)
% increase
500
0
Time to slow wave peak (s)
C
mPFC - Reuniens
Slow wave-spindle PAC
Frequency (Hz)
% increase
100
0
Time to slow wave peak (s)
D
Coupling strength
mPFC-mPFC
mPFC-Reu
Count
Slow wave-spindle coupling (SI)
E
***
mPFC-Reu (SI)
mPFC-mPFC (SI)
F
Coupling phase
90°
0.25
±180°
0°
-90°
mPFC-mPFC
mPFC-Reu
mPFC-Reu slow wave delays
G mPFC (LFP)
500 µV
Slow wave
(0.5-2 Hz)
200 µV
Reu (LFP)
200 µV
Slow wave
(0.5-2 Hz)
100 µV
200 ms
H
***
Reu
slow
wave
peak
Count
Time to mPFC SW peak (s)
I
Count
Median delay times (s)
Slow wave-ripple phase locking
J
mPFC (LFP)
0.5 mV
Slow-wave
(0.5-2 Hz)
0.5 mV
Hipp. (LFP)
1 mV
SWR
r.m.s.
(150-200 Hz)
100 µV
200 ms
K
***
90°
0.35
±180°
0°
-90°
0.5 mV
50 µV
50 ms